Received July 30, 2020, accepted August 27, 2020, date of publication August 31, 2020, date of current version September 15, 2020.

Digital Object Identifier 10.1109/ACCESS.2020.3020748

A New Probability Density Function for Minimizing Geometric Dilution of Precision in Location-Aware Wireless Communications

JOHN D. ROTH, (Senior Member, IEEE), MURALI TUMMALA, (Senior Member, IEEE), AND JOHN C. MCEACHEN, (Member, IEEE)

Department of Electrical and Computer Engineering, Naval Postgraduate School, Monterey, CA 93943, USA

Corresponding author: John D. Roth (jdroth@nps.edu)

The views expressed in this document are those of the authors and do not reflect the official policy or position of the U.S. Department of Defense or the U.S. Government.

ABSTRACT Cellular site planners have long used propagation models for optimizing an architecture deployment strategy. The foundation of these models are a plethora of theoretical results that all contribute to a probabilistic understanding of this phenomenon. In lower-band frequencies, coverage and propagation phenomena were sufficient considerations for legacy infrastructure deployment; however, as cellular technology probes uncharted millimeter wave spectra and beyond, it is natural to inquire as to whether other metrics could contribute to an informed infrastructure deployment. As the benchmark goals for positioning accuracy grow more ambitious and location-aware communications becomes a reality, we argue that localization accuracy should also play a prominent role in cellular infrastructure deployment planning. To this end, we submit a new closed-form probability density function (PDF) to characterize the angular difference of a pair of base stations and a mobile terminal. The importance of the angular difference is demonstrated by showing that the Cramér-Rao lower bound for localization is solely a function of it and measurement accuracy. Further, we submit a computationally tenable algorithm for producing the required PDF. To demonstrate the power of the density, we show some base station deployments that are guaranteed to yield geometrically favorable environments for positioning. Finally, we demonstrate how this new distribution outperforms numerical analysis when planning wireless network architecture deployment for location-aware communications.

INDEX TERMS 5G mobile communications, Cramér-Rao bounds, estimation theory, location estimation, millimeter wave communication.

I. INTRODUCTION

5G New Radio (NR) promises to deliver an unparalleled level of submeter location accuracy [1], [2]. This new access to high precision information begs the question of how it can be utilized and has drawn significant attention in the research [1], [3]–[9]. Location information has its pedigree in emergency services support [2], [10], but new hyper accurate information has opened the aperture for what is possible. A myriad of use cases across the protocol stack have been proposed [1].

In the physical layer, it has been shown that large capacity gains can be had via location-aware adaptive systems [11], beam training can be improved [12], prediction of channel quality is possible [13], and other notable gains in areas such as multiple input multiple output (MIMO) systems are possible [9].

Innovative use cases for location information persist up the protocol stack and include location-aware scheduling [9], geographical routing [14], industrial internet-of-things [2], and geriatric assisted living [8] among a plethora of others.

Indeed, to meet this growing appetite for decimeter-level accuracy, multifarious methods of enabling location-services in NR are being standardized in the NR positioning protocol "a" (NRPPa) [15]. To this end, the Third Generation Partnership Project (3GPP) has recycled legacy methods such as uplink and downlink time difference of arrival and enhanced cell ID. New functionality such as multicell round trip time and uplink/downlink angle of arrival are poised to push the accuracy, latency, and time-to-first-fix boundaries even further. The 3GPP investment in location services, however, doesn't end with abstract functionality. A major network

The associate editor coordinating the review of this manuscript and approving it for publication was Cunhua Pan.

architectural change of including a radio access network (RAN)-based location management component (LMC) has been codified with the aim of advancing the aforementioned localization metrics [16].

Given the significant architectural investment in the so-called location-based services (LBS), informed deployment of physical infrastructure becomes increasingly important. In particular, it has been shown that significant variability in positioning performance can result depending on the underlying architecture due to the phenomenon of geometric dilution of precision (GDoP) [17], which is independent of the particular positioning methodology employed. In other words, a sophisticated positioning system can be made inaccurate by not being mindful of how positioning architecture is physically deployed. Therefore, understanding the best physical deployment strategy of such a system could be the difference between meeting critical accuracy requirements or not. For applications where human life is a concern, such as autonomous vehicles [1], [3], [18]–[20], the level of confidence in location accuracy must be extremely high.

To this end, we contribute to a stochastic theory of location-based Fisher information available in wireless networks. Here, we are specifically concerned with how to best physically deploy nodes (e.g., next-generation node Bs (gNBs) in 5G) in order to minimize geometric dilution of position estimation accuracy. Since regular polygons are relatively common in cellular architectures [21]–[24], we assume that a cell is either polygonal or well-approximated by one. Given this polygon $\mathcal{P}$, within which users are expected to be uniformly distributed, we then approach the question of how to optimally place fixed measurement points $\mathbf{p}_i$ (e.g., a gNB, picocell, femtocell, or other complementary infrastructure) by way of developing a probability density for the a novel measure: angular difference. Angular difference serves as a convenient proxy for GDoP. In fact, as will later be shown, by choosing to utilize a proxy such as angular difference insights to the geometric climate for positioning can be gleaned which would otherwise be unavailable via standard numerical methods. This is largely due to the highly sensitive nature of GDoP. Indeed, we may make two points to be located as close as we like while also making the difference in their GDoPs as large as we like. This instability in the objective function makes it insuitable for numerical methods.

In contrast, our exact and closed-form density completely captures the required Fisher information and informs architectural deployment in networks, such as 5G, which lean so heavily on location services. More specifically, this work details an algorithm that yields the aforementioned closed-form expression of the cumulative distribution function (CDF) of angular differences $\Delta\theta$. From this follows a probability density function (PDF) since closed-form derivatives exist for all of the terms in the CDF. We demonstrate the power of this density by presenting some base station deployments which yield geometrically favorable climates for location accuracy. Additionally, we demonstrate how using this distribution can succeed in informing a better architectural deployment for LBS where numerical methods which calculate GDoP would otherwise fail.

We compose this correspondence of our work as follows. In the subsequent section we begin by discussing selected work related to our contribution. The related work can be grouped into three categories, work related to distance distributions, mathematical problems which relate to the problem at hand, and localization research. In all cases, we endeavor to make clear the differences in the existing literature and our present contribution. Next, we develop the theory that undergirds our algorithm in Section III. Specifically, we evaluate the Cramér-Rao lower bound (CRLB) for the given scenario and develop its relationship to a closely related and more analytically tractable measure: angular difference. It is this angular difference for which we develop a distribution with the understanding that it analogously describes the GDoP phenomenon. With the aforementioned relationship established we develop the theory of these dynamics in Sections IV and V. In Section VI, we then discuss the calculations necessary for execution of the proposed algorithm. The algorithm and its implications are presented subsequently in Sections VII and VIII. Notable implications that we highlight are the effect of several key geometries of infrastructure deployment as well as a more clear picture of the geometric climate for positioning than calculating GDoP directly. Finally, concluding remarks are given in our Section IX dénouement.

II. RELATED WORK

Geometrically-motivated probability distributions have enjoyed significant attention across a range of research disciplines, which, in modernity, have included wireless networks. The preponderance of the literature focuses on distance distributions, due to a natural connection to path loss. Example point processes for which distance distributions have been described include the Poisson and binomial point processes [25], [26]. Additionally, random node distance distributions in arbitrary finite areas are dealt with in [27]. From a fixed relay point in a square, the joint distribution of distances to a source and destination node are presented in [28]. Finally, distance distributions for regular polygons from a fixed point to the k^{th} nearest neighbor are presented in [24]. This work is closely related to ours. From [24], we adopt the algorithmic framework and apply it to the problem of developing a density applicable to Fisher information. Also closely related to our work is [29], which derives a lower bound for GDoP utilizing a polygonal construct. While the author described a specific bound where equality held only in the center of the polygon, our work builds on theirs by analogously describing the probability of a certain GDoP (by way of angular differences) given a uniformly distributed position for arbitrary fixed measurement point locations. We believe that our results build on those presented in [29] by presenting a more general picture of the expected geometric effect on positioning in a given area by utilizing the novel measure of angular differences.

A similar search of the mathematics literature reveals classical problems closely related to the one presented here. For instance, triangulations of planar surfaces have long been of interest both in applied areas such as computer graphics and also in pure math [30], [31]. The closest relation an existing mathematical problem has to the present one is polygon triangle picking. In this problem, regular polygons with N sides are considered. Three points are chosen from random inside the polygon with the goal of describing the distribution of the area of the convex hull of the points (i.e., the resulting triangle). Distributions are known for all $N \geq 3$ [32], [33]. While this problem is similar to the one considered by our research, it is also fundamentally different in several ways. First, in our application, two of the points are fixed ($\mathbf{p}_1$ and $\mathbf{p}_2$) and a third is random ($\mathbf{x}$) vice three random points. Second, as we will soon see, we are interested in understanding a different phenomenon than the distribution of areas.

Other research that shares in the vein of localization is the vast amount of work that developed distance estimation algorithms and position estimation. This is a mature field with seminal works [34] from which have grown various application-specific studies such as bistatic radar [35], [36]. In this research genre, the primary concern is estimating some number of parameters, such as directions of arrival, and fusing these parameter estimates into a position estimate. In the case of fusion, all of the published methods are subject to error magnification or, conversely, reduction, due to the complementary physical position of the measurement nodes. This geometric effect is well-understood under deterministic constraints. For instance, if the relative locations of the measurements nodes and the target are known, the geometric contribution to the accuracy of the position estimate can be precisely calculated [37]. Our work differs from this body of research in that it pursues an extension of the deterministic theory, which is agnostic to the method of parameter fusion utilized. We therefore do not compare our work directly with existing state-of-the-art methods in fusion or parameter estimation.

In a cellular network various nodes are typically deployed with coverage (or some other proxy) as the primary metric to be optimized without exact knowledge of where a subscriber is located. Coverage is then optimized over a particular area as opposed to a specific location. However, as location services grow in importance, we argue that the quality of the measurement geometry should also be considered during network deployment. To the best of our knowledge, what has not been considered is how to optimally[1] place measurement nodes given a coverage area where the distribution of user equipment (UE) requiring location-services is not known. We approach this question by deriving a closed-form expression for the distribution of Fisher information which, in turn, captures the GDoP given a set of measurement nodes with known location.

[1]We make note that here, and throughout the remainder of the manuscript, when we qualify something as optimal we do so in the context of accurate location-based services.

III. THE RELATIONSHIP BETWEEN ANGULAR DIFFERENCE DISTRIBUTIONS AND FISHER INFORMATION

In this section we highlight the novel relationship of the angular difference to the GDoP. This relationship is fundamental to the remainder of the paper. By addressing this quantity which runs parallel to GDoP we admit analytical tractability.

To begin, consider the impact of geometry on a localization scenario involving K fixed points $\{\mathbf{p}_1, \mathbf{p}_2, \ldots, \mathbf{p}_K\} \in \mathbb{R}^2$ with known location. These fixed points make a position estimate $\hat{\mathbf{x}}$ of an object at location $\mathbf{x}$, all in some finite region $\mathcal{P} \in \mathbb{R}^2$. For our purposes, we consider a position estimate based on time of arrival (ToA) such that each fixed point supplies a distance estimate corrupted by zero-mean white Gaussian noise $[\hat{d}_1, \hat{d}_2, \ldots, \hat{d}_K]^T$ from which the position estimate $\hat{\mathbf{x}}$ is derived via some function $f([\hat{d}_1, \hat{d}_2, \ldots, \hat{d}_K]^T) : \mathbb{R}^K \to \mathbb{R}^2$.

An important quantity required in the subsequent derivation requires us to admit the variable $\theta_{\mathbf{p}_i,\mathbf{x}} \in \mathbb{R}$ which is the angle subtended by an arbitrary line passing through $\mathbf{p}_i$ and the line containing both $\mathbf{p}_i$ and $\mathbf{x}$ such that for all $\mathbf{p}_i \in \{\mathbf{p}_1, \mathbf{p}_2, \ldots, \mathbf{p}_K\}$ the arbitrary lines are all parallel (cf. Figure 1).

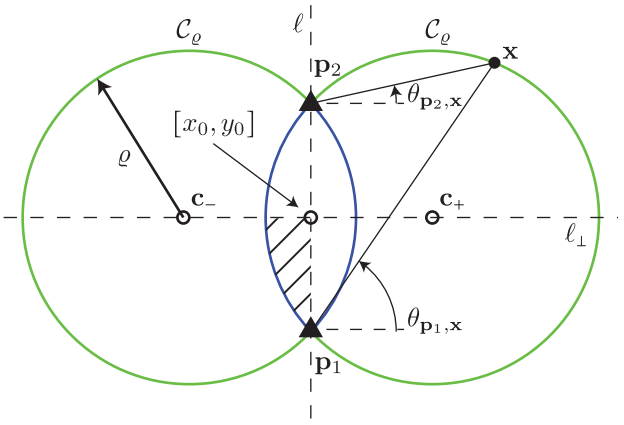

FIGURE 1. Given two fixed points $\mathbf{p}_1$ and $\mathbf{p}_2$ the set of all points where $\Delta\theta$ is constant is the boundary of the intersection or union of two disks. When $\Delta\theta \in [-\pi, -\pi/2)$ only the arcs of the circles that form the lens is valid. When $\Delta\theta \in (-\pi/2, 0)$ the complement of the lens is valid. The area computed by the integral in (12) is the hatched region of $\mathcal{C}_\varrho$, hence its preceding constant.

Definition 1: The angular difference between fixed points $\mathbf{p}_i$ and $\mathbf{p}_j$ relative to $\mathbf{x}$ is given as $\Delta\theta_{ij} = \theta_{\mathbf{p}_i,\mathbf{x}} - \theta_{\mathbf{p}_j,\mathbf{x}}$.

The importance of angular difference to the present application is central to this work and thus merits focus.

Theorem 1: Given an efficient unbiased estimator $f([\hat{d}_1, \hat{d}_2, \ldots, \hat{d}_K]^T) = \hat{\mathbf{x}}$ where $\mathrm{var}(\hat{d}_i) = \varsigma^2$, the expected value of $|\hat{\mathbf{x}} - \mathbf{x}|$ is only a function of $\Delta\theta_{ij}$.

Proof: Fisher information readily describes the best possible performance of an unbiased estimator. Given the constraints, the Fisher information matrix (FIM) is well-known

to be [37]

$$\mathbf{I}=\frac{1}{\varsigma^2}\sum_{i=1}^{K}\begin{bmatrix}\cos^2(\theta_{\mathbf{p}_i,\mathbf{x}}) & \cos(\theta_{\mathbf{p}_i,\mathbf{x}})\sin(\theta_{\mathbf{p}_i,\mathbf{x}})\\ \sin(\theta_{\mathbf{p}_i,\mathbf{x}})\cos(\theta_{\mathbf{p}_i,\mathbf{x}}) & \sin^2(\theta_{\mathbf{p}_i,\mathbf{x}})\end{bmatrix}. \tag{1}$$

The trace of $\mathbf{I}^{-1}$ then gives the CRLB, a standard benchmark for all unbiased parameter estimates [38]. Since the distance measurement error is assumed to be independent and identically distributed (IID) across all fixed points the scaling factor ς^{-2} can be pruned from (1) to yield the Fisher information of only the underlying geometry. The trace of the inverse of this matrix is commonly referred to as the GDoP, a purely geometric analog to the CRLB. The required trace of the inverse of this matrix is obtained as

$$\mathrm{Tr}\left(\varsigma^2\mathbf{I}^{-1}\right)=\frac{2K}{\sum_{i=1}^{K}\sum_{j=i+1}^{K}\left(1-\cos\left(2\Delta\theta_{ij}\right)\right)}, \tag{2}$$

the exact derivation of which is presented in Appendix B. From (2) it is clear that the subject quantity is only a function of $\Delta\theta_{ij}$. ∎

We pause here to emphasize the importance of (2) which directly links GDoP (the measure of interest) to $\Delta\theta_{ij}$ our novel metric. Throughout this manuscript we will demonstrate how utilizing $\Delta\theta$ as a measure in place of GDoP can better inform wireless network infrastructure deployment when planning such a deployment with LBS in mind.

Corollary 1: The expected value of $|\hat{\mathbf{x}}-\mathbf{x}|$ *is maximized when the fixed points* $\{\mathbf{p}_1,\mathbf{p}_2,\ldots,\mathbf{p}_K\}$ *are collinear with* $\mathbf{x}$.

To see this note that

$$\lim_{\Delta\theta_{ij}\to n\pi}\mathrm{Tr}(\varsigma^2\mathbf{I}^{-1})=\infty \tag{3}$$

for any $n\in\mathbb{Z}$ since each of the summands in the denominator of (2), $1-\cos(2\Delta\theta_{ij})$, is zero for the given condition. By Definition 1, the referenced condition occurs when $\theta_{\mathbf{p}_i,\mathbf{x}}=\theta_{\mathbf{p}_j,\mathbf{x}}+n\pi$. Since all $\{\mathbf{p}_1,\mathbf{p}_2,\ldots,\mathbf{p}_K\}\in\mathcal{P}$ (i.e., the distance between all points are finite), the subject angles are only equal when the aforementioned collinearity is satisfied.

Corollary 2: The expected value of $|\hat{\mathbf{x}}-\mathbf{x}|$ *is minimized when the fixed points* $\{\mathbf{p}_1,\mathbf{p}_2\}$ *are orthogonal with* $\mathbf{x}$.

To see this, consider that (2) is minimized when

$$\Delta\theta_{ij}=(2n+1)\frac{\pi}{2} \tag{4}$$

for any $n\in\mathbb{Z}$ which occurs only when the convex hull of the involved points is a right triangle such that the longest side ℓ is the one containing both $\mathbf{p}_1$ and $\mathbf{p}_2$ (i.e., the fixed points are orthogonal to the point to be measured).

In an effort to scope the following results, we now restrict our attention to the various geometries of $\{\mathbf{p}_1,\mathbf{p}_2,\mathbf{x}\}\in\mathcal{P}$ and how that geometry affects the GDoP environment within the polygon $\mathcal{P}$. Our choice of presenting the following analysis for two fixed points is made in order to simplify the analysis without sacrificing generality. To see this, consider (2) which expresses GDoP as a function of pairwise angular differences $\Delta\theta_{ij}$. A method of expressing $\Delta\theta_{ij}$ can then be iteratively applied to achieve the desired distribution for K fixed measurement points.

In order to inform optimal placement of the fixed points for some $\mathbf{x}$ uniformly distributed in $\mathcal{P}$, we now require a distribution for angular difference $\Delta\theta_{ij}$.

IV. ANGULAR DYNAMICS

We begin our approach towards a distribution of $\Delta\theta_{12}$ with some preliminaries. Specifically, we present angular behavior in an infinite region $\mathcal{P}$. This case is then extended in the sequel to a finite $\mathcal{P}$.

We then proceed by way of an area-based derivation inspired by [24]. Specifically, we define an area where we can guarantee that $\Delta\theta_{12}$ will observe certain limits. The ratio of this area to the area of $\mathcal{P}$ (in the finite case) gives way to the required distribution.

A. ANGULAR TOPOGRAPHY

Without loss of generality, we subsequently drop the subscripts of $\Delta\theta$ and limit $\Delta\theta\in[-\pi,0)$.

Lemma 1: The set $\mathcal{A}_1$*, that satisfies for all* $\mathbf{x}\in\mathcal{A}_1$ *then* $\Delta\theta\in[-\pi,-\pi/2)$*, is the intersection of two disks* $\mathcal{D}_+\cap\mathcal{D}_-$ *which both contain* $\mathbf{p}_1$ *and* $\mathbf{p}_2$.

Proof: Let $\mathcal{C}_\varrho$ be a a circle of radius ϱ such that $\{\mathbf{p}_1,\mathbf{p}_2\}\in\mathcal{C}_\varrho$ and ℓ be the line that contains $\mathbf{p}_1$ and $\mathbf{p}_2$. Referring to Figure 1, the inscribed angle theorem guarantees that all the points in $\mathcal{C}_\varrho$ that lie on one side of ℓ result in a fixed $\Delta\theta$ for all $\mathbf{x}\in\mathcal{C}_\varrho\subset\mathcal{A}_1$. Note that for a given ϱ that there are two such $\mathcal{C}_\varrho$ that can contain both fixed points, thus for a given $\Delta\theta$, the set of $\mathbf{x}$ which satisfy Definition 1 is the union of these two circular arcs (outlined by the blue boundary in Figure 1). Here, we imbue each circle which contains the arcs with an orientation $\pm$ for notational convenience. The radius of these circles $\varrho\in[|\bar{\ell}|/2,\infty)$ (where $|\bar{\ell}|$ denotes the magnitude of the line segment $\bar{\ell}$ with $\mathbf{p}_1$ and $\mathbf{p}_2$ as its endpoints) is parameterized by $\Delta\theta$ such that a larger $\Delta\theta$ implies a smaller ϱ. Therefore, we can extend the intersection to include the interior of the circles which has a symmetric lens shape. The width of the lens is parameterized by the specific value of $\Delta\theta$ such that as it approaches $-\pi$ the circles increase in radius and their intersection approaches the line segment which contains $\mathbf{p}_1$ and $\mathbf{p}_2$ as endpoints $\bar{\ell}$. Alternatively, as $\Delta\theta$ approaches $-\pi/2$ then the intersection approaches a circle with $\mathbf{p}_1$ and $\mathbf{p}_2$ as antipodal points. ∎

Lemma 2: The set $\mathcal{A}_2$ *which satisfies for all* $\mathbf{x}\in\mathcal{A}_2$ *then* $\Delta\theta\in[-\pi/2,0)$ *is the union of two disks* $(\mathcal{D}_+\cup\mathcal{D}_-)\setminus\mathcal{D}_{|\bar{\ell}|/2}$.

Proof: We first have from Lemma 1 that for $\Delta\theta=-\pi/2$ that $\mathcal{A}_1=\mathcal{D}_{|\bar{\ell}|/2}$ which we can clearly not include, hence the set difference. The reasoning for the intersection follows the same argument as the previous lemma. The resulting $\mathcal{C}=\partial\mathcal{A}_2$ for which $\Delta\theta$ is constant in the required range is given in green in Figure 1. The major difference here, however, is that a larger $\Delta\theta$ implies a *larger* ϱ and thus the resultant disks are combined via *union*. ∎

With these two lemmas we can fully describe the required set $\mathcal{A}=\mathcal{A}_1\cup\mathcal{A}_2$.

B. ANGULAR PARAMETERIZATION

Having established the general nature of $\mathcal{A}$, we now require a mapping that relates $\Delta\theta$ to each $\mathcal{C}_\varrho$. As $\mathcal{C}_\varrho$ is parameterized by both its radius ϱ and its center $\mathbf{c} = [x_c, y_c]^T$, we first consider the relationship between $\Delta\theta$ and $\mathbf{c}$.

Lemma 3: The centers $\mathbf{c}_-$ and $\mathbf{c}_+$ are given by

$$\begin{aligned} x_c &= x_0 \pm m\cos(\vartheta)/(2\tan(\Delta\theta)) \\ y_c &= y_0 \pm m\sin(\vartheta)/(2\tan(\Delta\theta)) \end{aligned} \tag{5}$$

where ϑ is the angle between a horizontal axis and $\ell_\perp$ (the perpendicular bisector of $\bar{\ell}$) and $[x_0, y_0]^T$ is the intersection of ℓ and $\ell_\perp$.

Proof: Note that the center of each $\mathcal{C}_\varrho$ will always lie on the perpendicular bisector $\ell_\perp$ of the radical line ℓ. Proceeding inductively, consider the special case where ℓ is $x = 0$ and $\mathbf{p}_1 = [0, 0]^T$. The perpendicular bisector $\ell_\perp$ is then $y = m/2$ where $m = \| \mathbf{p}_1 - \mathbf{p}_2 \|_2$. Now, combining the following three equations that represent the angular difference, the circle through $\mathbf{p}_2$, and the circle through $\mathbf{p}_1$, respectively

$$\Delta\theta = \arctan\left(\frac{m-y}{-x}\right) - \arctan\left(\frac{y}{x}\right), \tag{6}$$

$$r^2 = (x - x_c)^2 + (y - m/2)^2, \tag{7}$$

and

$$r^2 = x_c^2 + (m/2)^2 \tag{8}$$

we arrive at

$$x_c = \frac{\pm m}{2\tan(\Delta\theta)} \tag{9}$$

where the $\pm$ has been included to account for circle orientation. Since $y_c = m/2$ for all values of $\Delta\theta$, we have established the relationship between $\mathbf{c}$ and $\Delta\theta$ for the special case when ℓ is $x = 0$, $\mathbf{p}_1 = [0, 0]^T$, and $\mathbf{p}_2 = [0, m]^T$. By interpreting (9) as the magnitude of the displacement of $\mathbf{c}$ from the midpoint $[x_0, y_0]^T$ along $\ell_\perp$ we can calculate the vertical and horizontal components of that displacement when $\vartheta \neq 0$ via multiplication of (9) by $\sin\vartheta$ or $\cos\vartheta$ respectively. Finally, adding the midpoint $[x_0, y0]^T$ completes the proof. ∎

Lemma 4: The radius is related to $\Delta\theta$ via

$$\varrho = -\frac{m}{2}\csc(\Delta\theta). \tag{10}$$

Proof: The lemma quickly follows from substitution of (9) into (8). ∎

Theorem 2: The area of $\mathcal{A}$ is obtained by

$$|\mathcal{A}| = \frac{m^2}{2}\left((\Delta\theta + \pi)\csc^2(\Delta\theta) - \cot(\Delta\theta)\right), \tag{11}$$

where $\Delta\theta \in [-\pi, 0)$.

Proof: Consider the hatched area in Figure 1. Making use of polar coordinates, the area of $\mathcal{A}$ is calculated by

$$|\mathcal{A}| = 4\int_{x_c}^{\varrho} r' \arccos\left(\frac{-x_c}{r'}\right) dr' \tag{12}$$

where the leading constant 4 takes the area of the subject region and multiplies it to give the total area of $\mathcal{A}$. Evaluating (12) and then substituting (5) and (10) appropriately gives the area as per the theorem. ∎

C. DYNAMICAL OBSERVATIONS

We have thus established the topology of $\mathcal{A}$ relative to $\Delta\theta$. By (5) the centers of $\mathcal{C}_\varrho$ displace from $[x_0, y_0]^T$ nonlinearly in $\Delta\theta$. The magnitude of displacement from $[x_0, y_0]^T$ is infinite when $\Delta\theta = -\pi$, zero when $\Delta\theta = -\pi/2$, and then infinite again in the opposite direction when $\Delta\theta = 0$. Thus when $\Delta\theta = -\pi$ then $\mathcal{A}$ is the line segment $\bar{\ell}$. Similarly, when $\Delta\theta = 0$ then $\mathcal{A}$ is the entire plane $\mathbb{R}^2$.

For all values of $\Delta\theta$, both centers $\mathbf{c}_\pm$ travel along $\ell_\perp$. The radius ϱ also behaves nonlinearly in $\Delta\theta$. At either extreme of $\Delta\theta$ it is infinitely large and achieves its minimum $m/2$ at $\Delta\theta = -\pi/2$.

Corollary 3: The area of $\mathcal{A}$ is monotonically increasing on the interval $\Delta\theta \in [-\pi, 0)$.

By evaluating the derivative of (11) as

$$\begin{aligned} &\frac{d}{d\Delta\theta}|\mathcal{A}| \\ &= \frac{m^2}{2}[\cot^2(\Delta\theta) + \csc^2(\Delta\theta) - 2\frac{(\Delta\theta+\pi)\cos(\Delta\theta)}{\sin^3(\Delta\theta)} + 1], \end{aligned} \tag{13}$$

it can be seen that

$$\frac{d}{d\Delta\theta}|\mathcal{A}| > 0, \quad \forall\Delta\theta \in [-\pi, 0). \tag{14}$$

The monotonicity of the area function is an important property if we are to derive the distribution of angles. Consider the problem of determining the probability that an angle is no larger than a particular value, in other words, its cumulative distribution $F(\Delta\theta|\mathbf{p}_1, \mathbf{p}_2)$ is queried for the subject value. Let $\mathcal{P}$ be the set of all points which we allow $\mathbf{x}$ to assume, and let the probability that $\mathbf{x}$ be any given point in $\mathcal{P}$ be equal. From this, it follows that the CDF

$$F(\Delta\theta|\mathbf{p}_1, \mathbf{p}_2) = \frac{|\mathcal{A}|}{|\mathcal{P}|} \tag{15}$$

if

$$\mathcal{A} \cap \mathcal{P} = \mathcal{A}. \tag{16}$$

Clearly, this equality will not hold for a finite $\mathcal{P}$ and all values of $\Delta\theta$. We therefore turn to the problem of calculating $|\mathcal{A}|$ for arrangements where (16) is not satisfied.

V. CONSTRAINED DYNAMICS

It will be that $\mathcal{A} \cap \mathcal{P} \neq \mathcal{A}$ for many values of $\Delta\theta$ if $|\mathcal{P}|$ is finite, therefore an approach to calculating $|\mathcal{A}|$ when equality in (16) does not hold is necessary.

A. CONSTRAINT DEFINITION

Let the subscript of $\mathcal{P}_\rho$ represent the radius of the circumcircle of $\mathcal{P}$ centered at the origin in $\mathbb{R}^2$. Recall the earlier assumption that the region in question is a regular polygon.

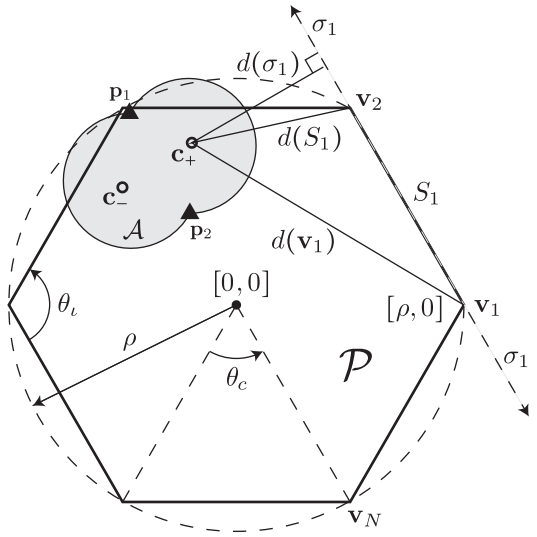

FIGURE 2. The instantaneous distances for σ_1 are presented here for the special case where $d(\sigma_1) \neq d(S_1)$. This inequality is a result of the positioning of the fixed points relative to S_1.

Regular polygons are well represented in wireless networks justifying their theoretical basis [23], [39]. In this case, $\mathcal{P}$ is fully parameterized by its circumcircle radius ρ and its number of sides N. An example $\mathcal{P}$ is shown in Figure 2 for the special case of $N = 6$. $\mathcal{P}$ has vertices $\mathbf{v}_1 \dots \mathbf{v}_N$ numbered anticlockwise where $\mathbf{v}_1 = [\rho, 0]^T$. This family of polygons enjoys many established results from which we will draw on. Such results include formulations of its area $|\mathcal{P}|$, interior angle θ_ι, and central angle θ_c.

B. DEFINITION OF DISTANCES

The rotational symmetries of regular polygons belong to the dihedral group and, as noted by [24], provide a unique opportunity for algorithmic exploitation. Development of this strategy for the present application will require several preliminaries that rest upon three different ideas of distance, which we define subsequently.

Definition 2: The instantaneous distance $d(\cdot)$ is a Euclidean distance from either of the centers $\mathbf{c}_\pm$ to one of three points[2]*:*

1) *the closest point of the line σ_n containing vertex $\mathbf{v}_n$ and $\mathbf{v}_{n+1}$ (denoted $d(\sigma_n)$),*
2) *the closest point of the line segment S_n containing vertex $\mathbf{v}_n$ and $\mathbf{v}_{n+1}$ (denoted $d(S_n)$), or*
3) *the vertex $\mathbf{v}_n$ (denoted $d(\mathbf{v}_n)$).*

These distances are a function of the geometry of the fixed points and $\Delta\theta$ and are presented graphically in Figure 2 for an example $\Delta\theta$. Of particular note is that the equality $d(S_n) = d(\sigma_n)$ will not hold in general as is demonstrated in Figure 2.

[2]Note that subscript arithmetic for parts of $\mathcal{P}$ is performed modularly such that the subscript index is a member of $\{1, 2, \dots, N\}$.

1) INSTANTANEOUS DISTANCES

To begin, let $\mathbf{R}_n : \mathbb{R}^2 \to \mathbb{R}^2$ be a linear isometry which applies a rotation about the origin with magnitude equal to the central angle θ_c of $\mathcal{P}$ n times. In other words, this transformation is a rotational member of the dihedral group which cycles the order of the vertices n times. Points given by the circle centers $\mathbf{c}_\pm$ are thus mapped to coordinates $\mathbf{c}_\pm^{\circlearrowleft n} = [x^{\circlearrowleft n}, y^{\circlearrowleft n}]^T$. The map $\mathbf{R}_n$ can be represented as a matrix operation via

$$\mathbf{c}_\pm^{\circlearrowleft n} = \mathbf{R}_n^{-1}\mathbf{c}_\pm \tag{17}$$

where

$$\mathbf{R}_n = \begin{bmatrix} \cos(n\theta_c) & -\sin(n\theta_c) \\ \sin(n\theta_c) & \cos(n\theta_c) \end{bmatrix}. \tag{18}$$

Lemma 5: The instantaneous side distance $d(\sigma_n)$ is given by

$$d(\sigma_n) = \left|(\rho - x_c^{\circlearrowleft n})\sin(\theta_\iota/2) - y_c^{\circlearrowleft n}\cos(\theta_\iota/2)\right|. \tag{19}$$

Proof: Proceeding inductively, the instantaneous side distance of either center $\mathbf{c}_\pm$ to the infinite line σ_1 that contains vertices $\mathbf{v}_1$ and $\mathbf{v}_2$ is

$$d(\sigma_1) = \left|(\rho - x_c^{\pm})\sin(\theta_\iota/2) - y_c^{\pm}\cos(\theta_\iota/2)\right| \tag{20}$$

where $[x_c^\pm, y_c^\pm]^T$ is defined as in (5). To see this observe the following geometry.

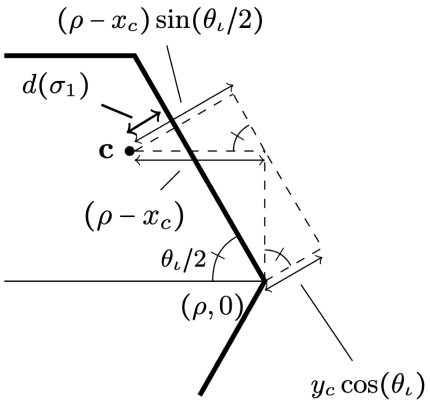

To complete the proof we now require generalization of (20) to all the polygon sides. Following the strategy developed by [24], we can accomplish this via the rotational symmetries of the dihedral group. First we rotate $\mathbf{c}$ n times and then apply (20). ∎

Lemma 6: The instantaneous vertex distance $d(\mathbf{v}_n)$ is given by

$$d(\mathbf{v}_n) = \sqrt{(\rho - x_c^{\circlearrowleft n})^2 + (y_c^{\circlearrowleft n})^2}. \tag{21}$$

Proof: Consider the specific vertex distance $d(\mathbf{v}_1)$ which is clearly given by

$$d(\mathbf{v}_1) = \sqrt{(\rho - x_c)^2 + y_c^2}. \tag{22}$$

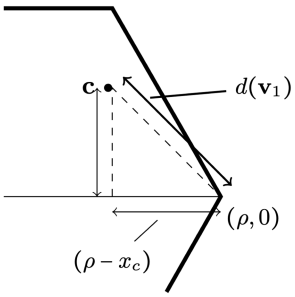

Again exploiting the rotational symmetries of the dihedral group (22) generalizes to (21). ■

Consider a line l_n which is perpendicular to σ_n and contains a point $\mathbf{c}$. Denote the intersection of l_n and σ_n as $\mathbf{l}_n$.

Definition 3: A constrained perpendicular projection $\wp_n$ of a point $\mathbf{c}$ *onto a line segment S_n is given as the point in S_n which is closest to* $\mathbf{l}_n$.

Note that under certain conditions $\wp_n$ will be a point in the interior of S_n whilst in other circumstances $\wp_n$ will be an endpoint of S_n. For example, consider Figure 2. The the constrained perpendicular projection $\wp_1$ of $\mathbf{c}_+$ onto S_1 is $\mathbf{v}_2$. Conversely, the intersection of S_2 and a perpendicular line containing $\mathbf{c}_+$ is nonempty and thus $\wp_2$ for $\mathbf{c}$ onto S_2 is a point between $\mathbf{v}_3$ and $\mathbf{v}_2$.

Lemma 7: The instantaneous segment distance $d(S_n)$ is given by

$$d(S_n) = \| \wp_n - \mathbf{c}^{\circlearrowleft_n} \|_2 \ . \tag{23}$$

A constrained perpendicular projection can be expressed as a parameterized vector

$$\wp = \mathbf{v}_{n+1} + \tau(\mathbf{v}_n - \mathbf{v}_{n+1}), \tag{24}$$

where

$$\tau = \max(0, \min(1, (\mathbf{c} - \mathbf{v}_{n+1})\hat{\bullet}(\mathbf{v}_n - \mathbf{v}_{n+1}))), \tag{25}$$

where $\hat{\bullet}$ represents the vector dot product that is normalized such that $\mathbf{v}_n \hat{\bullet} \mathbf{v}_n = 1$ for any $|\mathbf{v}_n|$. The maximum and minimum functions ensure that $0 \leq \tau \leq 1$. The vector projection performed by $\hat{\bullet}$, measures how far along σ_n, referenced to $\mathbf{v}_{n+1}$ $\wp_n$ appears. By definition and the rotational symmetries of the dihedral group the instantaneous segment distance is established. ■

Here, we highlight that, since the centers travel along $\ell_\perp$ according to $\Delta\theta$, all of the aforementioned distances can be thought of as being a function of $\Delta\theta$. We will use this idea subsequently for deriving important intervals of $\Delta\theta$.

2) ABSOLUTE ANGULAR DISTANCES

We have previously established that as $\Delta\theta$ ranges from $-\pi$ to 0 that the set $\mathcal{A}$ grows. In the sequel, our derivation of the distribution of Fisher information will be piecewise with each region of the CDF being calculated according to the shape of $\mathcal{A} \cap \mathcal{P}$. These regions are found with the following notions of distance.

Definition 4: The absolute angular distance $D(\cdot)$ is the smallest value of $\Delta\theta$ where the intersection of the boundary of $\mathcal{A}$ and the argument to D is not empty.

Lemma 8: The absolute angular side distance $D(\sigma_n)$ is given by a value of $\Delta\theta$ such that

$$d(\sigma_n) = \varrho \tag{26}$$

subject to the constraint that S_n (which is a subset of σ_n) is on the same side of ℓ as the referenced $\mathbf{c}$.

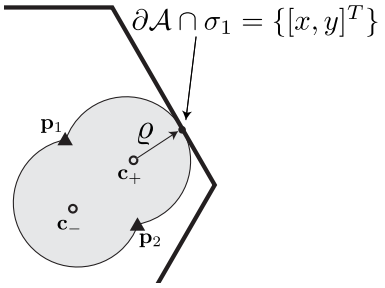

Proof: The required $\Delta\theta$ is the one where the intersection is exactly one point. When the intersection is exactly one point it will also be that the radius of the circle on the affected side will be the same as (19). Also, we again appeal to the dihedral rotational symmetries (which in this case are embedded in $d(\sigma_n)$).

A final qualifying constraint is required since $\mathcal{A}$ is not a disk and so a pathological geometry could lead to an incorrect result. To see this consider

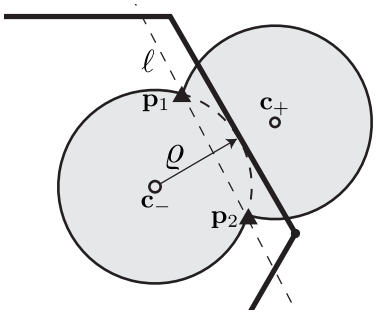

where clearly $d(\sigma_n) = \varrho$, yet per Definition 4 the intersection $\partial\mathcal{A} \cap \sigma_n$ is not a single point. However, if ℓ is respected as a boundary, the above pathology is easily discarded. ■

Note that (26) is transcendental, and thus has no closed-form solution. The solution can, however, be efficiently obtained via numerical solvers.

Lemma 9: The absolute angular vertex distance $D(\mathbf{v}_n)$ is given by the $\Delta\theta$ such that

$$d(\mathbf{v}_n) = \varrho \tag{27}$$

subject to the constraint that $\mathbf{v}_n$ is on the same side of ℓ as the referenced $\mathbf{c}$.

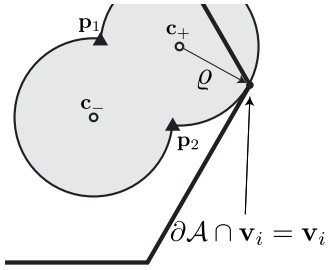

Proof: The proof of this lemma follows closely that of the previous. From Definition 4 we are primarily concerned about the boundary of $\mathcal{A}$. Therefore, the subject intersection will only be nonempty when the equality in (27) is satisfied. Additionally, the usual reliance on the dihedral rotational symmetries is required due to the inclusion of $d(\mathbf{v}_n)$. The final constraint is again needed in order to prevent pathologies similar to those described in the proof to Lemma 8. ∎

Lemma 10: The absolute angular segment distance $D(S_n)$ is given by

$$D(S_n) = \begin{cases} D(\sigma_n) & \text{if } \wp_n \notin \{\mathbf{v}_n, \mathbf{v}_{n+1}\} \\ \min\left(D(\mathbf{v}_n), D(\mathbf{v}_{n+1})\right) & \text{o.w..} \end{cases} \tag{28}$$

Proof: The argument for this proof parallels the argument for Lemma 7. As the circle expands the first point on S_n that it will touch will always be $\wp_n$. Therefore, if $\wp_n$ is a vertex then $D(S_n)$ is measured to that vertex. Alternatively, if $\wp_n$ is not an endpoint of S_n then we measure the distance instead to that point since it is the first one the circle will touch as it grows. ∎

3) ANGULAR HULL DISTANCE

Finally, for reasons which will later become apparent, we require the $\Delta\theta$ which marks when a center passes outside of $\mathcal{P}$.

Definition 5: The angular hull distance $D(H_n)$ is the $\Delta\theta$ where $\mathbf{c}$ is contained by σ_n and $\Delta\theta > -\pi/2$.

Lemma 11: The angular hull distance is given by

$$D(H_n) = \arctan\left(\frac{m\cos(n\vartheta)}{2\tan(\pm x_c^{\circlearrowleft_n} \mp x_\perp)}\right) \tag{31}$$

subject to the constraint that $-\pi/2 \leq \Delta\theta$.

Recall that angular dynamics dictate that as $\Delta\theta$ starts at $-\pi$ the centers will be outside of the circle, they will then enter the circle along $\ell_\perp$ and then exit again in opposite directions. Since we are only concerned with when they *exit*, we omit the first half of their journey with the constraint noted in the lemma.

Having discarded half of the values of $\Delta\theta$ the required distance is found by setting x_c in (5) equal to the coordinate $x_\perp$ of the intersection of $\ell_\perp$ and σ_n. This equality is graphically depicted here for the specific example of $D(H_1)$.

This could alternatively be accomplished with y_c and $y_\perp$ to the same effect. Again, the dihedral symmetries are required. ∎

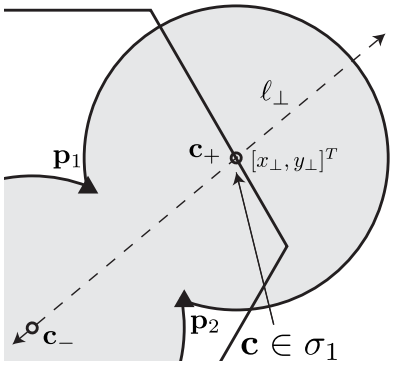

C. DATA STRUCTURE OF DISTANCES

The absolute distances play a central part in developing the piecewise structure of the CDF. Thus the nature of their organization requires attention.

Let the angular distances be stored in a vector $\mathbf{d} = [\mathbf{d}_{S,-}, \mathbf{d}_{S,+}, \mathbf{d}_{\mathbf{v},-}, \mathbf{d}_{\mathbf{v},+}, \mathbf{d}_{H,-}, \mathbf{d}_{H,+}]$ where $\mathbf{d}_{S,\pm} = [D(S_1), \ldots, D(S_N)]$ corresponds to the absolute angular side distances from $\mathbf{c}_\pm$. The other entries in $\mathbf{d}$ are similarly represented. The vector $\mathbf{d}$ then contains $6N$ values, some of which may be empty if no $\Delta\theta \in [-\pi, 0)$ satisfies the distance function. For instance, in the example presented in Lemma 11, $D(S_1) = D(\sigma_1) = \varnothing$ for the leftmost center $\mathbf{c}_-$.

VI. CONSTRAINED AREAS

In the sequel, we will calculate the area $\mathcal{A} \cap \mathcal{P}$ by starting with the area of $\mathcal{A}$ and removing portions of $\mathcal{A}$ that lie outside of $\mathcal{P}$. The areas that need to be calculated in order to accomplish this can be divided into two types: those when $\mathbf{c}$ is not a member of the area being calculated and when it is a member of that area.

A. WHEN c IS NOT A MEMBER OF THE AREA UNDER CALCULATION

In this subsection we consider first only scenarios where $\mathbf{c}$ is not part of the area which is being calculated. Formulation of a partial set of the areas required in this region was first introduced by [24]. However, proper calculation of the area $\mathcal{A} \cap \mathcal{P}$ requires new derivation and introduction or adaptation.

As shown in Figure 3, these areas come in two general types: B and C.

Definition 6: B_n is the annular segment which lies inside $\mathcal{C}_\varrho$ and σ_n and does not contain $\mathbf{c}$. Further, if $d(S_n) \neq d(\sigma_n)$ it does not contain any point closer to $\mathbf{c}$ than $\min(d(\mathbf{v}_n), d(\mathbf{v}_{n+1}))$.

The subject area B_n must be removed from the area of $\mathcal{A}$ anytime a particular line segment S_n is breached by $\mathcal{A}$ since this area lies outside $\mathcal{A} \cap \mathcal{P}$. The annular nature described when $d(S_n) \neq d(\sigma_n)$ is an artifact of computation, but is handled appropriately as described in the next section.

Lemma 12: The area of B_n is calculated via (29)*, shown at the bottom of the next page.*

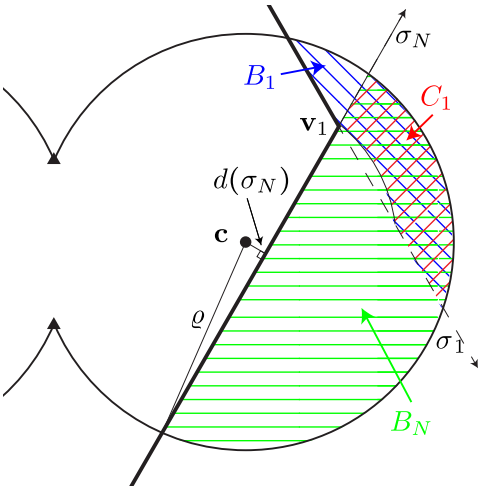

FIGURE 3. The two area types required to calculate the area of $\mathcal{A} \cap \mathcal{P}$ when $\mathbf{c}$ is inside the polygon are B_n and C_n. Note the annular shape of B_1 and C_1 (but not B_N) due to the position of $\mathbf{c}$ relative to $\mathbf{v}_1$.

By first integrating in polar coordinates with respect to θ' from the line that is a perpendicular bisector of σ_n to the point where $\mathcal{A}$ intersects with σ_n. Along r' the integral extends from $d(S_n)$ to ϱ. The preceding constant doubles this value to arrive at the desired area. ■

Definition 7: C_n is the annular segment which lies inside $\mathcal{A}$, σ_n, and σ_{n-1}. Further, if $d(S_n) \neq d(\sigma_n)$ it does not contain any point closer to $\mathbf{c}$ than $\min(d(\mathbf{v}), d(\mathbf{v}_{n+1}))$.

This area is double counted when both B_n and B_{n-1} are subtracted from $\mathcal{A}$. Once calculated it can be used to account for this phenomenon.

Lemma 13: The area of C_n is calculated via (30)*, shown at the bottom of the page.*

To calculate C_n, we first divide the desired region (shown in Figure 3) into two separate regions with the line that contains $\mathbf{c}$ and $\mathbf{v}_n$. These areas are described by the two integrals in (30). In each integral the angular extent that should be integrated over spans $[\phi_1, \arccos(d(\sigma_n)/r')]$ in the first integral and $[\phi_2, \arccos(d(\sigma_{n-1})/r')]$ in the second. In general neither ϕ_1 nor ϕ_2 is known. However, in evaluating the integrals we are left only with their sum which remains constant $\phi_1 + \phi_2 = \pi - \theta_\iota$. ■

At times, our algorithm will require the area of the annular hole cut by C_n.

Definition 8: The area of the annular hole cut by C_n is $\tilde{C}_n$.

Lemma 14:

$$\tilde{C}_n = 2 \int_{d(\sigma_k)}^{d(S_k)} \int_0^{\arccos\left(\frac{d(\sigma_k)}{r'}\right)} r' d\theta' dr' \tag{32}$$

where the index k is given as

$$k = \begin{cases} i & d(\sigma_{n-1}) < d(\sigma_n) \\ i-1 & o.w.. \end{cases} \tag{33}$$

By observation, the required area is easily derived via the presented double integral. The only item requiring special care is identifying which line and side to use for the limits of integration. This selection can be made based on whether σ_n or σ_{n-1} is closer to $\mathbf{c}$. The rule presented in the lemma is easily verified also by inspection. ■

Note that this area will be zero when $d(S_n) = d(\sigma_n)$. The closed-form expression of $\tilde{C}_n$ can be obtained as in B by substituting the limits of integration and $d(\sigma_k)$ appropriately into (29).

Consider now that (30) will not produce a result that is easily interpreted when $\mathbf{c}$ is outside exclusively either σ_n or σ_{n-1} as seen in Figure 4. This is because when $\mathbf{c}$ is in the subject region the ϕ_1 and ϕ_2 sum to a different constant, namely θ_ι. Therefore, a new area is required.

Definition 9: D_n is the area bounded by σ_n, σ_{n-1}, and $\mathcal{A}$.

Lemma 15:

$$D_n = C_n + \frac{\pi}{N}\left(\varrho^2 - d(\mathbf{v}_n)^2\right) - \frac{\theta_\iota}{2}\left(\varrho^2 - d(\mathbf{v}_n)^2\right). \tag{34}$$

The presented formulation removes the last term from C_n (30) and replaces it with the last term in (34) in order to correct for the new value of $\phi_1 + \phi_2$. ■

$$\begin{aligned} B_n &= 2 \int_{d(S_n)}^{\varrho} \int_0^{\arccos\left(\frac{d(\sigma_n)}{r'}\right)} r' d\theta' dr' \\ &= \varrho^2 \arccos\left(\frac{d(\sigma_n)}{\varrho}\right) - d(\sigma_n)\sqrt{\varrho^2 - d(\sigma_n)^2} - d(S_n)^2 \arccos\left(\frac{d(\sigma_n)}{d(S_n)}\right) + d(\sigma_n)\sqrt{d(S_n)^2 - d(\sigma_n)^2} \end{aligned} \tag{29}$$

$$\begin{aligned} C_n &= \int_{d(\mathbf{v}_n)}^{\varrho} \int_{\phi_1}^{\arccos\left(\frac{d(\sigma_n)}{r'}\right)} r' d\theta' dr' + \int_{d(\mathbf{v}_n)}^{\varrho} \int_{\phi_2}^{\arccos\left(\frac{d(\sigma_{n-1})}{r'}\right)} r' d\theta' dr' \\ &= \frac{\varrho^2}{2}\left(\arccos\left(\frac{d(\sigma_n)}{\varrho}\right) + \arccos\left(\frac{d(\sigma_{n-1})}{\varrho}\right)\right) - \frac{d(\mathbf{v}_n)}{2}\left(\arccos\left(\frac{d(\sigma_n)}{d(\mathbf{v}_n)}\right) + \arccos\left(\frac{d(\sigma_{n-1})}{d(\mathbf{v}_n)}\right)\right) \\ &\quad + \frac{d(\sigma_n)}{2}\left(\sqrt{d(\mathbf{v}_n)^2 - d(\sigma_n)^2} - \sqrt{\varrho^2 - d(\sigma_n)^2}\right) + \frac{d(\sigma_{n-1})}{2}\left(\sqrt{d(\mathbf{v}_n)^2 - d(\sigma_{n-1})^2} - \sqrt{\varrho^2 - d(\sigma_{n-1})^2}\right) \\ &\quad - \frac{\pi}{N}\left(\varrho^2 - d(\mathbf{v}_n)^2\right) \end{aligned} \tag{30}$$

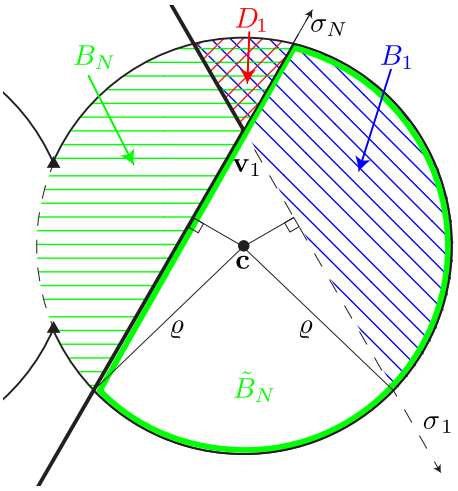

FIGURE 4. The two area types ($\tilde{B}_n$ and D_n) required to calculate the area of $\mathcal{A} \cap \mathcal{P}$ when $\mathbf{c}$ is outside the polygon, but has not crossed two lines σ_n and σ_m for $n \neq m$. In this example, $\mathbf{c}$ has crossed σ_N but not σ_1. Note that in this example calculating $\tilde{B}_N$ (the perimeter of which is outlined in bold green above) involves also knowing B_N. The area of B_1 is calculated as before per (29).

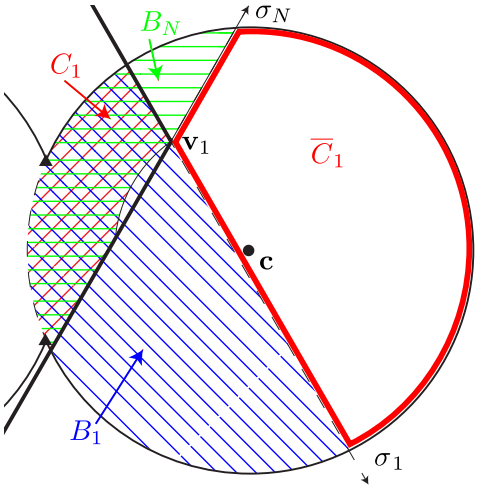

FIGURE 5. Here, $\mathbf{c}$ is a member of the region to be calculated. Given this scenario, $\overline{C}_1$ (whose perimeter is outlined in bold red) is calculated by first subtracting B_n and B_{n-1} from the total area of $\mathcal{A}$ and adding back in C_n and the area of the annular hole.

B. WHEN $\mathbf{c}$ IS A MEMBER OF THE AREA

When $\mathbf{c}$ is part of the region for which the area is being calculated, a different formulation is required. To begin, consider the case depicted in Figure 4. We desire to subtract the area outlined in green from $\mathcal{A}$; however, now that $\mathbf{c}$ is actually part of this area, the current formulation given in (29) calculates the area hatched in green.

Definition 10: $\overline{B}_n$ *is the circular complement of* B_n.

Lemma 16:

$$\overline{B}_n = \pi \varrho^2 - B_n. \tag{35}$$

The lemma easily follows by inspection. ■

Now, regard the case presented in Figure 5 where calculation of the area outlined in bold red $\overline{C}_n$ is required. Evaluation of (30) produces the area labeled C_1 in Figure 5 which is not required.

Definition 11: $\overline{C}$ *is the area bounded by* σ_{n-1}, σ_n, *and* $\mathcal{C}_\varrho$ *and also contains* $\mathbf{c}$.

Lemma 17:

$$\overline{C}_n = \pi \varrho^2 - B_n - B_{n-1} + C_n + 2 \int_{d(S_k)}^{d(\mathbf{v}_n)} \int_0^{\arccos\left(\frac{d(\sigma_k)}{r'}\right)} r' d\theta' dr', \tag{36}$$

where k *is defined as before in* (33).

The approach to calculating $\overline{C}$ is similar to that taken to calculate $\overline{B}$ in that the existing calculation methods are leveraged to achieve the required area. The only complication is again addressing the annular circular center, and is handled by the last double integral in the lemma. ■

Similar to (32), in the case where $d(S_k) = d(\mathbf{v}_n)$, the last double integral in the lemma evaluates to zero. The closed-form expression of the double integral is similar to (29) after the appropriate substitution of limits and $d(\sigma_k)$.

C. SUMMARY

The present section represents the culminating point of mathematical tool development in our work. As these areas, which when evaluated can all be given in closed form, represent the building blocks of our final CDF we pause to consider an important implication of the former fact.

Theorem 3: The PDF of $\Delta\theta$ *has a closed-form representation.*

The proof of this theorem follows from three facts. First, each of the areas presented in this section have a closed-form representation as given by the Leibniz integral rule. Second, Given all of the subject areas, one is able to always construct $\mathcal{A} \cap \mathcal{P}$. Finally, the PDF is the derivative of the CDF and the derivative of any closed-form expression is also guaranteed to be closed form. ■

At this juncture we would also reiterate why such a distribution is important. It is not that we desire to understand $\Delta\theta$ directly, rather it is the relationship of $\Delta\theta$ to GDoP (cf. (2)) introduced in Section IV that makes it useful. By calculating the distribution of angular distances we gain insight into the more cumbersome problem of determining the distribution of GDoP.

While we have now presented a calculus for obtaining the required pieces of the puzzle, it remains to be understood how they can be efficiently put together to obtain the required areas parameterized by $\Delta\theta$. An algorithmic agglomeration of the tools presented here is the main thrust of the next section.

VII. ALGORITHM

With all the necessary preliminaries addressed we now present an algorithm, derivative of the one introduced by [24], which produces the closed-form CDF (and by Theorem 3 implies the closed-form PDF) of the distribution of $\Delta\theta$ given two fixed measurement points $\{\mathbf{p}_1, \mathbf{p}_2\} \in \mathcal{P}$. Recall that just because the algorithm produces a distribution for two fixed measurement points doesn't mean that it is restricted to *only*

two measurement points. Should $K > 2$ points be utilized the algorithm can be implemented for each pair of the K points.

The algorithm is split into four parts: preliminary calculations, then determining the value of the CDF for three regions of support which comprise all possible values of $\Delta\theta$. The regions of support are defined for each $\mathbf{c}$ separately. For example, Region 1 could apply for $\mathbf{c}_-$ and Region 2 for $\mathbf{c}_+$ given a specific value of $\Delta\theta$. Further,he t regions of support are ordered, contiguous, and non-overlapping. Conventionally, the ordering of the regions is such that we assume initially that $\Delta\theta = -\pi$ and is varied up to its maximum $\Delta\theta = 0$. Along this progression, regions 1 through 3 are encountered in order while allowing for the non-existence of a region. In other words, if Region 2 doesn't exist then the Region 3 follows Region 1.

Each region is broken into various subregions which have a fixed method of calculation within their support. Subregions are defined by the vector $\mathbf{d}''$ of ordered unique distances. Once the boundary of each subregion is reached the method of calculation is updated. Similarly, the boundaries of the three regions adapt the algorithm used to update the method of calculation at each subregion.

A. ALGORITHM PREAMBLE

The algorithm first calculates the distance vector $\mathbf{d}$ (cf. Section V-C) and sorts the entries in ascending order into a new vector $\mathbf{d}'$. By sorting convention, we define the empty entry $\emptyset$ to be larger than any real-valued entry. The original indices are preserved in a separate and similarly permuted index vector $\mathbf{l}$ that will be utilized for dereferencing each of the entries in the sorted distance vector $\mathbf{d}'$ [24]. Let $g_N : \mathbb{R}\times\mathbb{Z}\times\mathbf{c}_\pm \to \{D(S_n), D(\mathbf{v}_n), D(H_n)\}$ be a dereferencing map for $\mathbf{d}'$ such that

$$g_N(\mathbf{d}'_n, \mathbf{l}, \mathbf{c}) = \begin{cases} D(S_n)|\mathbf{c}_- & \text{if } \mathbf{l}_n \le N \\ D(S_{n-N})|\mathbf{c}_+ & \text{if } N < \mathbf{l}_n \le 2N \\ D(\mathbf{v}_{n-2N})|\mathbf{c}_- & \text{if } 2N < \mathbf{l}_n \le 3N \\ D(\mathbf{v}_{n-3N})|\mathbf{c}_+ & \text{if } 3N < \mathbf{l}_n \le 4N \\ D(H_{n-4N})|\mathbf{c}_- & \text{if } 4N < \mathbf{l}_n \le 5N \\ D(H_{n-5N})|\mathbf{c}_+ & \text{if } 5N < \mathbf{l}_n \le 6N. \end{cases} \tag{37}$$

Given a distance entry in $\mathbf{d}'$, g_N essentially maps it to its type and number.

B. REGION 1

In order to better illustrate the mechanics of the proposed algorithm, we provide the specific geometry in Figure 6 as a complementary example to the following discussion. While this example is highlighted in the subsequent text, the multimedia accompanying this manuscript also illustrates the CDF development for this example via our algorithm. In particular, the example geometry is prescribed a circumradius $\rho = 1$ and the fixed points are positioned such that $\mathcal{P}$ is symmetric about ℓ. Specifically, $\mathbf{p}_1 = [0, 0]^T$ and $\mathbf{p}_2 = [-\sqrt{3}/4, 1/4]^T$.

Definition 12: Region 1 is the domain of $\Delta\theta$ that extends from $\Delta\theta = -\pi$ to the first hull distance (cf. Definition 5).

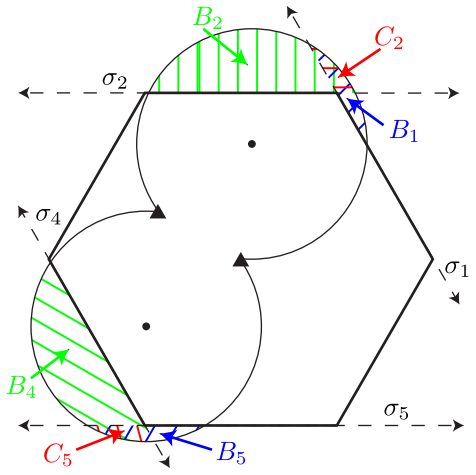

FIGURE 6. Here, $\mathcal{A}$ is presented for $\mathbf{d}''_2 \le \Delta\theta < \mathbf{d}''_3$ given the fixed point placement specified in Section VII-B where all the areas required for for calculation of $F_3^\dagger(\Delta\theta)$ are labeled.

Until the first entry in $\mathbf{d}'$, the CDF is accurately represented by $|\mathcal{A}|/|\mathcal{P}|$. After the first entry, $\Delta\theta \ge d'_1$, some area will need to be subtracted from $\mathcal{A}$ in order to calculate the area of $\mathcal{A} \cap \mathcal{P}$. This is correctly done by subtracting B_n when an entry dereferences to $D(S_n)$ and adding C_n when an entry dereferences to $D(\mathbf{v}_n)$. Further, addition of the annular hole $\tilde{C}_n$ is required if $D(S_k) = D(\sigma_k)$. This continues as long as the subsequent values of $\mathbf{d}'$ are the same. For instance, it may be that d'_1 and d'_2 have the same value, but dereference to a different distance. When a new value in $\mathbf{d}'$ is encountered, a new subregion of $F(\Delta\theta)$ is defined and new areas are additionally considered. These subregions are easily defined by deriving a vector $\mathbf{d}''$ by taking only the unique ordered values from $\mathbf{d}'$.

Referring now to the companion example in Figure 6, we note that the first two entries in $\mathbf{d}'$ are equal and dereference via g_6 to $D(S_1)$ and $D(S_4)$. The next four entries are also equal and dereference to $D(S_1)$, $D(S_5)$, $D(\mathbf{v}_2)$, and $D(\mathbf{v}_5)$. This process continues until $\Delta\theta \ge -\pi/2$ and $\mathbf{c}$ exits the polygon. The resulting unnormalized CDF which corresponds the the Region 1 support of $\Delta\theta$ would be

$$F^\dagger(\Delta\theta) = \begin{cases} F_1^\dagger(\Delta\theta) = |\mathcal{A}| & -\pi \le \Delta\theta < \mathbf{d}''_1 \\ F_2^\dagger(\Delta\theta) = |\mathcal{A}| \\ \quad -B_1 - B_4 & \mathbf{d}''_1 \le \Delta\theta < \mathbf{d}''_2 \\ F_3^\dagger(\Delta\theta) = |\mathcal{A}| \\ \quad -B_1 - B_2 - B_4 - B_5 \\ \quad +C_2 + C_5 & \mathbf{d}''_2 \le \Delta\theta < \mathbf{d}''_3 \\ F_4^\dagger(\Delta\theta) = |\mathcal{A}| \\ \quad -B_1 - B_2 - B_4 - B_5 \\ \quad +C_2 + C_5 \\ \quad -2B_3 + C_3 + C_4 & \mathbf{d}''_3 \le \Delta\theta < \mathbf{d}''_4 \\ \quad \vdots \end{cases} \tag{38}$$

where we have indicated by the superscript † that normalization by the area of the polygon is necessary to achieve a valid CDF. In the present example $\Delta\theta = \mathbf{d}''_4$ corresponds to the first hull distance and thus the start of Region 2.

C. REGION 2

Definition 13: The super-circumvertices (SCVs) of $\mathcal{P}$ are the points of intersection of all σ_n and the star polygon they form is the SCV hull.

Definition 14: Region 2 is supported by all $\Delta\theta$ greater than the Region 1 support, but where **c** *is still inside the SCV hull.*

The limits of Region 2 are efficiently found as the first and second hull distance. An example is given in Figure 4 where **c** has crossed σ_N, but not σ_1. Here, revisions of the previous calculations made in Region 1 are required based on the dereferenced hull distance. A revision of B_n is made for every $D(H_n)$ encountered. The revision includes first replacing the previously subtracted B_n and subtracting the correct area $\overline{B}_n$. Continuing in the same manner as in (38) the revision would take the form

$$F_j^{\dagger}(\Delta\theta) = F_{j-1}^{\dagger}(\Delta\theta) + B_n - \overline{B}_n. \tag{39}$$

Revision of C_n (and potentially also C_{n+1}) will also be necessary. The area is corrected as before by removing the erroneous C_n and adding the correct D_n via

$$F_j^{\dagger}(\Delta\theta) = F_{j-1}^{\dagger}(\Delta\theta) - C_n + B_{n-1} - D_n. \tag{40}$$

Revision of C_{n+1} is also necessary if $D(\mathbf{v}_{n+1})$ is less than the current last unique value of $\mathbf{d}'$. This revision is accomplished via

$$F_j^{\dagger}(\Delta\theta) = F_{j-1}^{\dagger}(\Delta\theta) - C_{n+1} + B_{n+1} - D_{n+1}. \tag{41}$$

In the companion example Region 2 is defined via

$$F^{\dagger}(\Delta\theta) = \begin{cases} \vdots \\ F_5^{\dagger}(\Delta\theta) = |\mathcal{A}| \\ \quad - B_1 - \overline{B}_2 - B_4 - \overline{B}_5 - 2B_3 \\ \quad + (B_1 - D_2) + (B_5 - D_5) \\ \quad + (B_3 - D_3) + (B_3 - D_4) \\ \qquad\qquad \mathbf{d}''_4 \le \Delta\theta < \mathbf{d}''_5 \\ \vdots \end{cases} \tag{42}$$

In this region $\mathbf{c}_+$ is inside the point of the star polygon defined by $\{\sigma_1, \sigma_2, \sigma_3\}$ and $\mathbf{c}_-$ is inside the point of the star defined by $\{\sigma_3, \sigma_4, \sigma_6\}$. Due to this positioning, B_2 and B_5 are replaced with $\overline{B}_2$ and $\overline{B}_5$ (cf. (35)) via (39). With the revision of B_2 and B_5 complete we now apply (40). Specifically, C_2 through C_5 are removed since the calculation now doesn't make sense given how (30) is defined. Further, Next, D_2 through D_5 is calculated (cf. (34)) and applied appropriately.

D. REGION 3

Definition 15: The SCV threshold γ_n is the $\Delta\theta$ where a center has passed through both σ_n and σ_{n-1}.

Region 3 begins when an SCV threshold has been exceeded.

Note that by this definition, it is possible for **c** to be outside the SCV hull but still within the SCV threshold. For instance, in Figure 5 **c** has crossed both σ_N and σ_1, thus it is outside of the SCV hull. However, it has only crossed the SCV threshold γ_1.

In this region, B is still revised as in (39); however, if a center has crossed γ_n, then C_n is revised differently than in (40). Specifically,

$$F_j^{\dagger}(\Delta\theta) = F_{j-1}^{\dagger}(\Delta\theta) - C_n + \overline{C}_n. \tag{43}$$

Again returning to the companion example illustrated in Figure 6, and continuing from (42), the remainder of the unnormalized CDF is given as

$$F^{\dagger}(\Delta\theta) = \begin{cases} \vdots \\ F_6^{\dagger}(\Delta\theta) = |\mathcal{A}| \\ \quad - B_1 - \overline{B}_2 - B_4 - \overline{B}_5 - 2B_3 \\ \quad + \overline{C}_2 + \overline{C}_5 \\ \quad + (B_3 - D_3) + (B_3 - D_4) \\ \qquad\qquad \mathbf{d}''_5 \le \Delta\theta < \mathbf{d}''_6 \\ F_7^{\dagger}(\Delta\theta) = |\mathcal{A}| \\ \quad - B_1 - \overline{B}_2 - B_4 - \overline{B}_5 - 2B_3 \\ \quad + \overline{C}_2 + \overline{C}_5 \\ \quad + (B_3 - D_3) + (B_3 - D_4) \\ \quad - 2B_6 + C_6 + C_5 \\ \qquad\qquad \mathbf{d}''_6 \le \Delta\theta < 0. \end{cases} \tag{44}$$

$F_6^{\dagger}$ shows the result of revision of C_2 and C_5 since both thresholds γ_2 and γ_5 have been exceeded. The final subregion $F_7^{\dagger}$ accounts for $\mathcal{A}$ expanding to include $\mathbf{v}_5$ and $\mathbf{v}_6$ (cf. 7).

E. IMPLEMENTATION

The CDF generation process detailed previously can be practically implemented as shown in the Algorithm 1. After the preamble, the outermost **while** loop indicates that the algorithm will run until a $\varnothing$ is reached in $\mathbf{d}'$. An empty entry is guaranteed to be present in $\mathbf{d}'$ since, for $\Delta\theta > -\pi/2$, **c** can pass through at most three lines σ_n. Therefore, there will be at least $N - 3$ empty entries in each $\mathbf{d}_{H,i}$.

The outermost **if** statement iterates through $\mathbf{d}'$ until an entry is found that is different from the previous entry. In this way, unique entries in $\mathbf{d}'$ define the j^{th} subregion $F_j^{\dagger}$ of the overall CDF as shown in (38), (42), and (44).

The **for** loop builds $F_j^{\dagger}(\Delta\theta)$ for each subregion by starting from $|\mathcal{A}|$ every iteration and adding and removing the necessary elements based on the first $j - 1$ entries in $\mathbf{d}'$. The necessary elements to remove and add are identified by dereferencing all $j - 1$ entries with g_N. The result of the

Algorithm 1 Angle Distributions in Regular Polygons

Calculate absolute distances and sort into $\mathbf{d}'$
$l = j = 1, \mathbf{d}'_0 = -\pi$
while $\mathbf{d}'_l \neq \varnothing$ **do**
  if $\mathbf{d}'_{l-1} \neq \mathbf{d}'_l$ **then**
    $F_j^{\dagger}(\Delta\theta) = |\mathcal{A}|$ where $\mathbf{d}'_{l-1} \leq \Delta\theta < \mathbf{d}'_l$
    for each $i \in \{1, \ldots, l-1\}$ **do**
      if $g_N(\mathbf{d}'_i) = D(S_n)$ **then**
        $F_j^{\dagger}(\Delta\theta) = F_j^{\dagger}(\Delta\theta) - B_n$
      else if $g_N(\mathbf{d}'_i) = D(\mathbf{v}_n)$ **then**
        $F_j^{\dagger}(\Delta\theta) = F_j^{\dagger}(\Delta\theta) + C_n$
        if $D(S_k) = D(\sigma_k)$ **then**
          $F_j^{\dagger}(\Delta\theta) = F_j^{\dagger}(\Delta\theta) + \tilde{C}_n$
        end if
      else
        $F_j^{\dagger}(\Delta\theta) = F_j^{\dagger}(\Delta\theta) + B_n - \overline{B}_n$
        if $\mathbf{d}'_l > D(\mathbf{v}_n)$ & $\mathbf{c} < \gamma_n$ **then**
          $F_j^{\dagger}(\Delta\theta) = F_j^{\dagger}(\Delta\theta)$
            $-C_n + B_{n-1} - D_n$
        else
          $F_j^{\dagger}(\Delta\theta) = F_j^{\dagger}(\Delta\theta)$
            $-1/2(C_n - \overline{C}_n)$
        end if
        if $\mathbf{d}'_l > D(\mathbf{v}_{n+1})$ & $\mathbf{c} < \gamma_{n+1}$ **then**
          $F_j^{\dagger}(\Delta\theta) = F_j^{\dagger}(\Delta\theta)$
            $-C_{n+1} + B_{n+1} - D_{n+1}$
        else
          $F_j^{\dagger}(\Delta\theta) = F_j^{\dagger}(\Delta\theta)$
            $-1/2(C_{n+1} - \overline{C}_{n+1})$
        end if
      end if
    end for
    $j = j + 1$
  end if
  $l = l + 1$
end while
$F(\Delta\theta) = |\mathcal{P}|^{-1} \bigcup_j F_j^{\dagger}(\Delta\theta)$

dereferencing map dictates which part of the **if/elseif/else** statement immediately inside the **for** loop is executed. If the **if** statement is executed, then $\mathcal{A}$ has extended beyond σ_n which warrants removal of the circular sector B_n from the overall area of $\mathcal{A}$. This condition can be invoked in all of the three regions.

If the **else if** clause is executed then $\mathcal{A}$ has extended beyond $\mathbf{v}_n$ and, as discussed previously, the region C_n will be double counted due to the removal of B_{n-1} and B_n. This step fixes the double removal of the area C_n from $\mathcal{A}$. A further step is sometimes necessary to add back in the annular hole via $\tilde{C}_n$. Similar to the **if** clause, the **if else** clause can be invoked in any of the three regions.

When a distance dereferences to a hull distance $D(H_n)$, the **else** clause is invoked. This condition will only execute in regions 2 and 3. When $\mathbf{c}$ exits the polygon (and $\Delta\theta \geq -\pi/2$), a mandatory revision of B_n and optional revisions of C_n and C_{n+1} is required due to the position of the center relative to the SCV thresholds and is handled by the two nested **if/else** conditions. Note that in the case where a hull distance is reached the implications for both $\mathbf{v}_n$ and $\mathbf{v}_{n+1}$ must be considered, hence the two **if/else** statements (cf. (40) and (41)).

The first **if** indicates that the γ_n has not been exceeded while the **else** statement indicates the complement. Note that since two **if/else** statements are considered for every hull distance that the factor of $1/2$ is included when calculating $\overline{C}_n$ so as not to double count it.

The final step after the **while** loop exits is a normalization and union of the computed areas such that a valid CDF is obtained. Since each F_j is defined only over its own non-overlapping domain, the union of subregions is equivalent to concatenation.

VIII. SOME EXAMPLE DISTRIBUTIONS

In this section we present CDFs for various geometries. Initially, geometries in $N = 6$ are explored due to the ubiquitous nature of the regular hexagon in wireless architecture. Next, a general equation and results for the CDF of a geometry where fixed points are vertices of a more general $\mathcal{P}_{\rho,N}$ are presented. In both of these cases, analytical CDFs realized by our algorithm precisely match empirically determined CDFs. Finally, an example use case of the distribution and a summary of the results are presented in the last two subsections.

A. SPECIAL CASE: SYMMETRIES OF THE DIHEDRAL GROUP

Here, we fix $N = 6$ and present results based on symmetries in the dihedral group of regular polygons with six sides. Since the rotational group members are exploited in the algorithm, the group members which are reflections are considered. As can be seen in Figure 7, there are two unique families of reflection generators: reflections about a line $R_{s,n}$, that bisects S_n and S_{n+3} and about a line $R_{v,n}$, that bisects vertices $\mathbf{v}_n$ and $\mathbf{v}_{n+3}$.

Consider the fixed points of Figure 7 given in magenta as $\triangle$. This geometry is symmetric about $R_{s,3}$ and $R_{v,2}$. One degree of symmetry is broken with the fixed points given in red as $+$. The opposite degree of symmetry is broken with the fixed points given in green as $\triangledown$. All three of the analytical CDFs resulting from the aforementioned fixed points are presented in Figure 8 and match empirical results exactly. While a generally similar behavior is noted in all of the tails of the distributions towards $\Delta\theta = -\pi$, the behavior is markedly different near $\Delta\theta = 0$.

If precise locationing is sought, then the fixed points must be positioned such that the expected CRLB is minimized. This happens when $\Delta\theta$ is $\pi/2$ modulo π (cf. Corollary 2). It may be observed that the magenta fixed points $\triangle$ provide the worst such environment with a heavy tail as $\Delta\theta$ approaches zero. The environment is improved when the

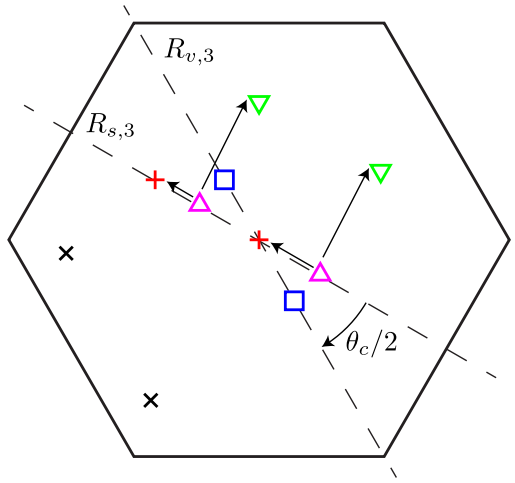

FIGURE 7. Presented here are the five scenarios presented in Figure 8. The marker color and shape represents the fixed points corresponding to each CDF in Figure 8 (which has the same marker color and shape). The fixed point positions are distributed to show the effect of symmetric positions on the resulting CDF. Reflection symmetries $\{R_{s,3}, R_{v,3}\}$ are denoted with dashed lines. Straight arrows represent orthogonal deviations from a particular symmetry.

fixed points are offset as in red $+$, and further so in green $\triangledown$, where it can be seen that the tails of the CDFs are reduced and probability density is shifted towards $-\pi/2$.

Consider next the fixed points of Figure 7 given in blue as $\square$. This geometry is symmetric about $R_{s,1}$ and $R_{v,3}$. Referring to the inset in Figure 8, it can be seen that this geometry affords some improvement when compared to that of $\triangle$ by minimizing the effect of the tail.

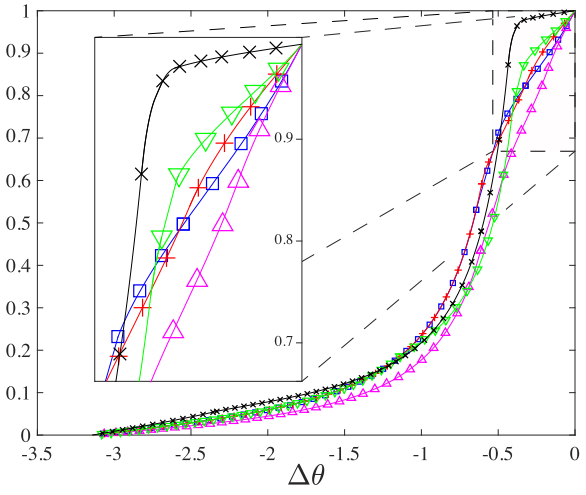

FIGURE 8. Presented are CDFs for symmetric placements of the fixed points. Curves with a particular color and marker shape map to placements with the same attributes in Figure 7. The figure is enlarged to highlight tail behavior.

As a final case, consider the fixed points that are symmetric about $R_{s,1}$ and given in black as $\times$. In this geometry, the fixed points are close enough to S_4 that $D(S_4) < -\pi/2$. Stated another way, $\mathcal{A}$ will breach $\mathcal{P}$ while it is still lens-shaped (cf. Figure 1). This results in $d(\sigma_4) < -\pi/2$ whereas in all previous examples all the solutions to (26) and (27) were greater than $-\pi/2$. This difference in solution location is the result the close proximity of the side and the fixed points. Regardless, by following the prescribed algorithm, the correct absolute angular distances are obtained and, again, the analytical and empirical result in Figure 8 match exactly.

When evaluated for positioning efficacy, this placement of fixed points realizes a dramatic improvement. This improvement is a result of elimination of the majority of points $\mathbf{x} \in \mathcal{P}$ where $\Delta\theta$ is large. This is possible due to its proximity to, in this instance, S_4 and results in the inspiration for the following special case.

B. SPECIAL CASE: $\mathbf{p}_1 = \mathbf{v}_1$ AND $\mathbf{p}_2 = \mathbf{v}_2$

In light of the favorable result obtained by the heavily asymmetric geometry of the fixed points given as black $\times$ in Figure 7, let $\mathbf{p}_1 = \mathbf{v}_1$ and $\mathbf{p}_2 = \mathbf{v}_2$. These fixed points yield both a favorable environment for positioning and are representative of how access points are often distributed in a cellular or wireless lattice [23], [40].

Further, the location of the fixed points makes the general equation for the CDF of $\Delta\theta$ concise. If N is odd then

$$F_j^{\dagger}(\Delta\theta) = \frac{|\mathcal{A}|}{2} - 2\sum_{n=2}^{j} B_n. \tag{45}$$

If N is even then

$$F_j^{\dagger}(\Delta\theta) = \frac{|\mathcal{A}|}{2} - 2\sum_{n=2}^{j} B_n - \delta[j - N/2 - 1]B_{N/2+1}. \tag{46}$$

Both equations are defined for $0 < j \leq \lfloor N/2 + 1 \rfloor$ and $\delta[]$ is the Kronecker delta function. Here, the only ingredient to the CDF is B_n the absolute vertex distance is the same for all vertices except for $\mathbf{v}_1$ and $\mathbf{v}_2$ since they are also $\mathbf{p}_1$ and $\mathbf{p}_2$. To see this, consider that any circle that contains three of the vertices must be the circumcircle and thus contain all of the vertices. Therefore, all of the vertices of $\mathcal{P}$ will be reached by $\mathcal{A}$ simultaneously.[3] Further, this happens exactly at the time when $F^{\dagger}_{\lfloor N/2+1 \rfloor}(\Delta\theta) = |\mathcal{P}|$ relieving any need to consider C_n. Additionally, because, in this special case, the algorithm ends once $\mathcal{C}_{\varrho}$ is a circumcircle then its center is inside of $\mathcal{P}$ relieving any need to consider areas in regions 2 or 3 (cf. Sections VII-C and VII-D).

The subject CDF is presented in Figure 9 for a triangle ($\triangle$), a square ($\square$), a pentagon ($+$), a hexagon ($\triangledown$), a dodecagon ($\times$), and a icositetragon ($\circ$).[4] The most notable trend is the shift of the CDF to favor higher values of $\Delta\theta$ as N increases. Recall that a favorable positioning environment is one where the expected $\Delta\theta$ is closest to $-\pi/2$. Given the subject geometry of fixed points, it can be easily determined empirically that the optimal $N = 4$. A triangle and a pentagon both shift their

[3] The exception being $\mathbf{v}_1$ and $\mathbf{v}_2$, which are the fixed points and thus always contained in $\mathcal{A}$ regardless of $\Delta\theta$.

[4] All polygons under considerations are regular.

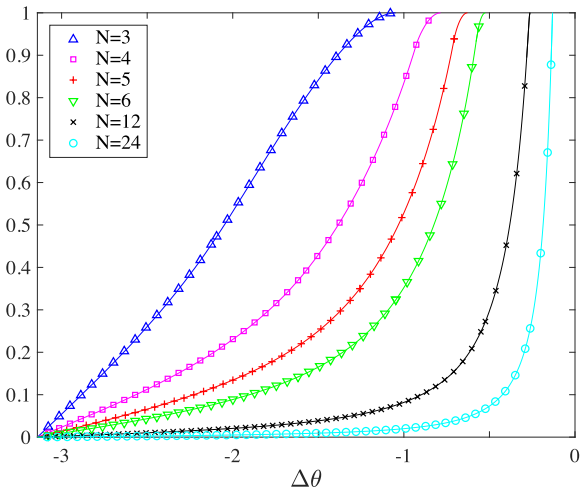

FIGURE 9. The CDFs when $\mathbf{p}_1 = \mathbf{v}_1$ and $\mathbf{p}_2 = \mathbf{v}_2$ for regular polygons with various number of sides N.

means farther away from the optimal expected $\Delta\theta = -\pi/2$. It also clear from the CDFs that the mean values will be monotonic in N when $N \geq 4$ guaranteeing that $N = 4$ is the optimal value for this particular configuration.

It is also interesting to inquire about the limiting behavior of the CDF as $N \to \infty$, in other words, as $\mathcal{P}$ approaches a circle. As $N \to \infty$ the shape of $\mathcal{P}$ approaches that of $\mathcal{A}$ which is in $\mathcal{P}$. In the limit, the points which define the polygon approach a circle. Since the side of $\mathcal{A}$ which is in the polygon is also a circle (46) and (45) simplify to

$$F(\Delta\theta) = \frac{1}{2}\frac{|\mathcal{A}|}{|\mathcal{P}|}, \qquad -\pi \leq \Delta\theta < 0. \tag{47}$$

However, since also the distance between the fixed points $m \to 0$ as $N \to \infty$, (47) becomes the Heaviside step function centered at $\Delta\theta = 0$. In this limiting case, (47) implies that $-\epsilon < \Delta\theta < 0$ for some small $\epsilon > 0$ and some sufficiently large N. This can also be approached more intuitively if one considers that if the distance between $\mathbf{p}_1$ and $\mathbf{p}_2$ goes to zero $\theta_{\mathbf{p}_1,\mathbf{x}} = \theta_{\mathbf{p}_1,\mathbf{x}}$. In other words, their angular difference to any third point $\mathbf{x}$ in $\mathcal{P}$ also approaches zero.

C. CELLULAR SITE PLANNING FOR LOCATION-BASED SERVICES

Next, we give an example of how one may plan a deployment of fixed-measurement nodes $\{\mathbf{p}_1, \mathbf{p}_2, \ldots, \mathbf{p}_K\}$ where $K > 2$ utilizing the distribution of angular difference. An alternative to using the distribution of angular differences proposed by this work is to numerically calculate the distribution of GDoP, which we will show to lead to inferior, or even incorrect results relative to our method. Further, we show the utility of our results for more than two fixed points.

In order to make this example as realistic as possible we again adopt the regular hexagon as $\mathcal{P}$ and place a single node at $\mathbf{v}_1$. This node could, for example, represent a macro base station (i.e., gNB) in a hexagonal lattice. We may now inquire as to where we may position a second node in order to maximize the precision of LBS. This area may be dictated by coverage requirements or some other metric. Motivated by the results in [17], [29] and in section VIII-A we propose that another vertex may produce the best results. We therefore calculate the distribution of the angular difference $\Delta\theta$ for secondary positions at $\mathbf{v}_2$, $\mathbf{v}_3$, or $\mathbf{v}_4$ (we may omit the remaining vertices from consideration by symmetry). If we evaluate these positions with the proposed method we can see from the CDFs in Figure 10 that $\mathbf{v}_3$ is a superior placement. The CDF shows that the distribution of angular differences will be less than when $\mathbf{p}_2 = \mathbf{v}_2$ and larger than when $\mathbf{p}_2 = \mathbf{v}_2$. Since GDoP is minimized when $\Delta\theta = -\pi/2$ (cf. (2)), it follows that when $\mathbf{p}_2 = \mathbf{v}_3$ is the best placement of $\mathbf{p}_2$ given the options.

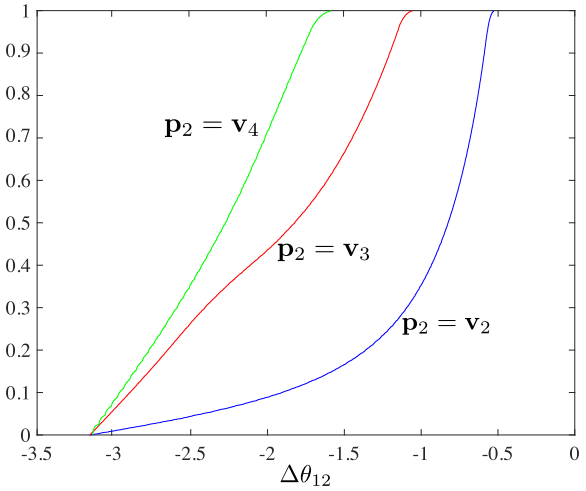

FIGURE 10. Given that $\mathbf{p}_1 = \mathbf{v}_1$ the distribution of $\Delta\theta_{12}$ is presented for various locations of $\mathbf{p}_2$.

Alternatively, the GDoP can be calculated for a sample of points drawn from the hexagon. Displaying these results as an empirical CDF or histogram is of limited value due to the widely varying range of the results, especially for those points along the line between $\mathbf{p}_1$ and $\mathbf{p}_2$. In fact, points that are on this line have an infinite GDoP and thus are difficult to incorporate into numerical analysis. This method is therefore highly sensitive to where the samples are drawn from in $\mathcal{P}$. Viewing contour plots of the GDoP in $\mathcal{P}$ (as done in [29]) is also of limited value. As can be seen in the top row of Figure 11, it is not obvious which contour plot should, on average, provide the best environment for LBS.

Here, we note that it would not be unreasonable to stop with only two nodes in an LBS architecture. In fact, the case for two nodes in cellular networks as an LBS enabler has been previously reported on [17]. Despite that with only two nodes the set of solution equations may be underdetermined, ambiguity can be resolved by alternate means such as cell boundaries or beamforming angle making two nodes a useful architecture for LBS.

Regardless, suppose now we require a third fixed measurement point $\mathbf{p}_3$. Intuition would suggest that the best location for $\mathbf{p}_3$ is $\mathbf{v}_5$ given the now fixed locations of $\mathbf{p}_2$ and $\mathbf{p}_1$.

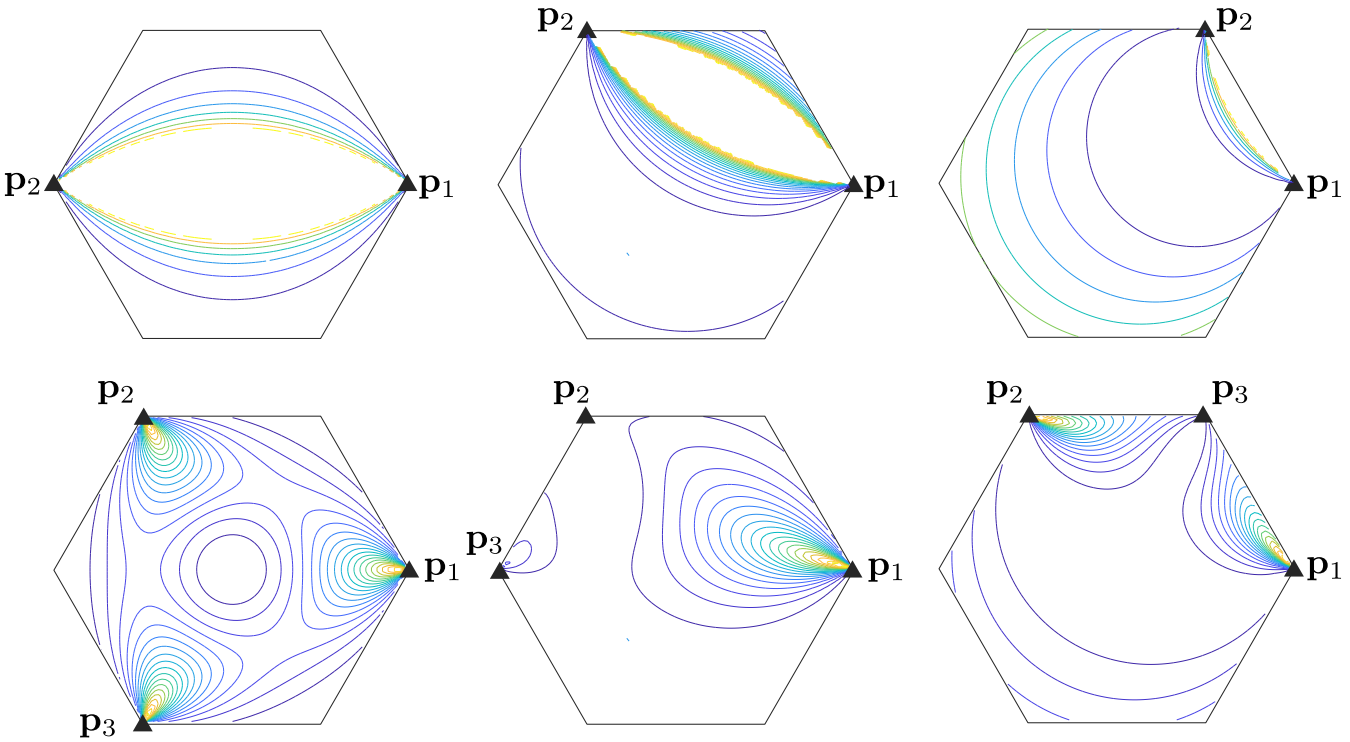

FIGURE 11. The top row of contour plots shows the GDoP for three different placements of $\mathbf{p}_2$. Using the proposed method it can be shown that the position where $\mathbf{p}_2 = \mathbf{v}_3$. Given the optimal location of $\mathbf{p}_2$, the bottom row shows the GDoP for various locations of $\mathbf{p}_3$. It can also be shown with the proposed distribution that the position where $\mathbf{p}_3 = \mathbf{v}_5$ is optimal.

In order to show this as correct, we can compare this placement to any of the other open vertices as an alternate candidates. Looking at the contour plots of the available candidates (where $\mathbf{v}_6$ can be omitted by symmetry) it is again not entirely obvious which placement results in the best geometric climate for all of $\mathcal{P}$. However, we can evaluate the distribution of angular differences resulting from $\mathbf{p}_1$ and $\mathbf{p}_3$ ($\Delta\theta_{13}$) and the distribution of angular difference resulting from $\mathbf{p}_2$ and $\mathbf{p}_3$ ($\Delta\theta_{23}$) when $\mathbf{p}_3$ is located at any of the open vertices. The angular differences between $\mathbf{p}_1$ and $\mathbf{p}_2$ are not needed since those locations have already been fixed.

In fact, no new computations are required since, by symmetry, any of those now required would be identical to one of the three distributions already available. For instance, if $\mathbf{v}_2$ is chosen as a location for $\mathbf{p}_3$ then $\Delta\theta_{13} = \Delta\theta_{23}$. The two CDFs are exactly the same as $\Delta\theta_{12}$ for $\mathbf{p}_2 = \mathbf{v}_2$ shown in Figure 10. Placing $\mathbf{p}_3$ at $\mathbf{v}_4$ results in two CDFs identical to those of $\Delta\theta_{12}$ for $\mathbf{p}_2 = \mathbf{v}_2$ and $\Delta\theta_{12}$ for $\mathbf{p}_2 = \mathbf{v}_4$. The only remaining placement to check is $\mathbf{v}_5$ and the resulting CDFs are identical to the CDF for $\Delta\theta_{12}$ for $\mathbf{p}_2 = \mathbf{v}_3$. By considering all combinations of CDFs it is clear that the $\mathbf{v}_5$ placement minimizes the expected GDoP for all of $\mathcal{P}$. This process can be iteratively applied if more than three fixed points are required.

We note that we have not shown that the above three placements are optimal in all of $\mathcal{P}$. Rather we have demonstrated, given constraints driven by other metrics, such as coverage, that the proposed distribution can discern geometry that will result in more precise LBS which would otherwise be difficult to obtain via numerical methods.

D. SUMMARY OF RESULTS

In this section we have utilized the distribution of angular differences to three ends. First, we evaluated several potential placements of infrastructure via this distribution. By choosing placements that orthogonally sampled the space available in $\mathcal{P}$ for $\mathbf{p}_1$ and $\mathbf{p}_2$ we developed an intuition for which locations may be superior. This intuition then motivated the special case of two adjacent vertices as $\mathbf{p}_1$ and $\mathbf{p}_2$. This distribution was notable since it was simple to express and allowed a straightforward way of evaluating the effect of changing the number of sides of $\mathcal{P}$. Finally, the efficacy of the developed theory was demonstrated in a cellular planning scenario. Here, the distribution of angular differences was used to find the best placement of $\mathbf{p}_1$ and $\mathbf{p}_2$ given constraints. The distribution was then used iteratively to show its utility for more than two fixed points. Notably, in this scenario it was shown how the distribution of angular differences provides a superior metric relative to numerically calculating average GDoP or evaluating contour plots of GDoP.

IX. CONCLUSION

In this research we have presented an alternative measure, angular difference $\Delta\theta$, to GDoP. Since GDoP is solely a function of angular difference, angular difference also describes the dilutive effects of physical geometry on LBS. However,

we have shown how it can be a superior method to directly calculating GDoP when one is concerned with the expected GDoP throughout an area served by a wireless network. While $\Delta\theta$ can be calculated numerically, we have additionally provided an algorithm for calculating it exactly in closed form, further strengthening it as an advantageous measure to GDoP.

In order to further draw out these advantages we have used it in a variety of scenarios culminating in a demonstration of how it can be used in conjunction with constraints to solve for an optimal placement of fixed point locations in a wireless network.

Given the modern ubiquitous nature of LBS, the increasingly strict standards-based requirements for localization accuracy, and the nascence of location-aware communications, we reckon that understanding angular distributions, is ever more important for optimization of wireless networks. Indeed, as was shown, this distribution fundamentally undergirds the FIM and thus the maximum achievable accuracy. Therefore, as localization methodologies sounds the theoretical limits, we must acknowledge and address the accuracy scaling effect of infrastructure layout.

As cellular technology grows into the millimeter-wave range and beyond, location services will play an ever increasingly central role in wireless networks. Among other areas, beam training, cell selection, and device-to-device communications will all benefit. By furthering our understanding of distributions related to positioning accuracy, modern wireless networks will be holistically advanced.

APPENDIX A
NOTATION (IN ORDER OF APPEARANCE)

$\mathcal{P}$	A regular polygon
N	Number of sides of a regular polygon
$\mathbf{p}_i$	i^{th} fixed measurement point
$\mathbf{x}$	True position to be estimated
$\hat{\mathbf{x}}$	Estimate of $\mathbf{x}$
K	Number of fixed measurement points
$\hat{d}$	A distance estimate
$\theta_{\mathbf{y},\mathbf{x}}$	Angle subtending locations $\mathbf{y}$ and $\mathbf{x}$ (cf. Fig. 1)
$\Delta\theta_{ij}$	Angular difference between $\theta_{\mathbf{p}_i,\mathbf{x}}$ and $\theta_{\mathbf{p}_j,\mathbf{x}}$
ς	Standard deviation of distance measurement noise
$\mathbf{I}$	Fisher information matrix
ℓ	Line that contains $\mathbf{p}_i$ and $\mathbf{p}_j$
$\bar{\ell}$	Line segment with $\mathbf{p}_i$ and $\mathbf{p}_j$ as its endpoints
$\mathcal{A}$	Area where $\Delta\theta_{ij}$ is less than some constant value
$\mathcal{D}$	A disk (i.e., a two-dimensional sphere)
$\mathcal{C}_\varrho$	Circle (i.e., the boundary of $\mathcal{D}$) with radius ϱ
$\mathbf{c} = [x_c, y_c]^T$	The center of $\mathcal{C}$
$\ell_\perp$	Perpendicular bisector of $\bar{\ell}$
ϑ	The angle subtending some horizontal axis and $\ell_\perp$
$[x_0, y_0]^T$	The intersection of ℓ and $\ell_\perp$
m	The distance between $\mathbf{p}_i$ and $\mathbf{p}_j$
θ_c	Central angle of $\mathcal{P}$
$\mathcal{D}$	The disk $\partial\mathcal{C}_\varrho$
θ_ι	The interior angle of $\mathcal{P}$
m	$\lvert\mathbf{p}_1 - \mathbf{p}_2\rvert$
ρ	Radius of the circumcircle of $\mathcal{P}$
$\mathbf{v}_i$	The i^{th} vertex of $\mathcal{P}$
θ_ι	The interior angle of $\mathcal{P}$
θ_c	The central angle of $\mathcal{P}$
$d(\cdot)$	The instantaneous distance
σ_i	The line containing $\mathbf{v}_i$ and $\mathbf{v}_{i+1}$
S_i	The i^{th} side of $\mathcal{P}$
$\mathbf{R}_n$	The linear isometric rotational transform of magnitude $n\theta_c$
$\wp$	A constrained perpendicular projection used in calculating $d(S_i)$
τ	A variable which takes on values in the probability simplex
$(\cdot)^{\circlearrowleft_n}$	The result of the product $\mathbf{R}_n(\cdot)$
$D(\cdot)$	Absolute angular distance
$[x_\perp, y_\perp]^T$	The intersection of $\ell_\perp$ and σ_1
$\mathbf{d}$	Vector of angular distances
$\mathbf{d}'$	$\mathbf{d}$ sorted in ascending order
$\mathbf{d}''$	The unique values of $\mathbf{d}'$ in ascending order
B_n, C_n, & D_n	The two general types of area calculations when $\mathbf{c} \in \mathcal{P}$
$\mathbf{l}$	Index vector that maps between $\mathbf{d}$ and its sorted counterpart $\mathbf{d}'$
g_N	Dereferencing map which takes a sorted distance to its type and number
γ_n	SCV threshold
R	Reflection symmetry of the dihedral group

APPENDIX B
DERIVATION OF THE TRACE OF $\varsigma^2\mathbf{I}^{-1}$

Define the matrix

$$\mathbf{A}_i = \begin{bmatrix} \cos^2(\theta_{\mathbf{p}_i,\mathbf{x}}) & \cos(\theta_{\mathbf{p}_i,\mathbf{x}})\sin(\theta_{\mathbf{p}_i,\mathbf{x}}) \\ \sin(\theta_{\mathbf{p}_i,\mathbf{x}})\cos(\theta_{\mathbf{p}_i,\mathbf{x}}) & \sin^2(\theta_{\mathbf{p}_i,\mathbf{x}}) \end{bmatrix}. \tag{48}$$

The full inverse of this matrix need not be computed since we only require the trace its inverse. Therefore, only the diagonal of the inverse is of interest. Since $\varsigma^2\mathbf{I}$ is a 2×2 matrix the trace of its inverse is simply given as (50), shown at the top of the next page.

The numerator quickly simplifies to

$$\mathrm{Tr}(\varsigma^2\mathbf{I}^{-1}) = \frac{K}{\det(\varsigma^2\mathbf{I})}. \tag{51}$$

Therefore,

$$\begin{aligned}\varsigma^2\mathbf{I} &= \mathbf{A}_1 + \mathbf{A}_2 + \cdots + \mathbf{A}_K \\ &= \begin{bmatrix} \cos^2\theta_1 + \cos^2\theta_2 + \cdots + \cos^2\theta_K & \cos\theta_1\sin\theta_1 + \cos\theta_2\sin\theta_2 + \cdots + \cos\theta_K\sin\theta_K \\ \cos\theta_1\sin\theta_1 + \cos\theta_2\sin\theta_2 + \cdots + \cos\theta_K\sin\theta_K & \sin^2\theta_1 + \sin^2\theta_2 + \cdots + \sin^2\theta_K \end{bmatrix}. \end{aligned} \tag{49}$$

$$\mathrm{Tr}(\varsigma^2\mathbf{I}^{-1}) = \frac{(\cos^2\theta_1 + \cos^2\theta_2 + \cdots + \cos^2\theta_K) + (\sin^2\theta_1 + \sin^2\theta_2 + \cdots + \sin^2\theta_K)}{\det(\varsigma^2\mathbf{I})}. \tag{50}$$

$$\begin{aligned}\det(\varsigma^2\mathbf{I}) &= (\cos^2\theta_1 + \cos^2\theta_2 + \cdots + \cos^2\theta_K)(\sin^2\theta_1 + \sin^2\theta_2 + \cdots + \sin^2\theta_K) \\ &\quad - (\cos\theta_1\sin\theta_1 + \cos\theta_2\sin\theta_2 + \cdots + \cos\theta_K\sin\theta_K)^2 \\ &= \sum_{i=1}^{K}\sum_{j=1}^{K}(\sin\theta_i\cos\theta_j)^2 - \left[\sum_{i=1}^{K}(\cos\theta_i\sin\theta_i)^2 + 2\sum_{i=1}^{K}\sum_{j=i+1}^{K}\cos\theta_i\sin\theta_i\cos\theta_j\sin\theta_j\right]. \end{aligned} \tag{53}$$

It now suffices to show that (cf. (2))

$$\det(\varsigma^2\mathbf{I}) = \frac{1}{2}\sum_{i=1}^{K}\sum_{j=i+1}^{K}(1 - \cos(2\Delta\theta_{ij})). \tag{52}$$

We begin directly by calculating the determinant as (53), shown at the top of the page.

All K terms of the second sum cancel with the same K terms in the first sum. After applying this first simplification we have

$$\begin{aligned}\det(\varsigma^2\mathbf{I}) &= \sum_{i=1}^{K}\sum_{j=1|j\neq i}^{K}(\sin\theta_i\cos\theta_j)^2 \\ &\quad - \left[2\sum_{i=1}^{K}\sum_{j=i+1}^{K}\cos\theta_i\sin\theta_i\cos\theta_j\sin\theta_j\right]. \end{aligned} \tag{54}$$

Now, consider the two identities

$$(\cos\theta_i\sin\theta_j)^2 + (\cos\theta_j\sin\theta_i)^2 = \frac{1}{2}(\sin^2(\theta_i+\theta_j) + \sin^2(\Delta\theta_{ij})) \tag{55}$$

and

$$2\cos\theta_i\sin\theta_i\cos\theta_j\sin\theta_j = \frac{1}{2}(\sin^2(\theta_i+\theta_j) - \sin^2(\Delta\theta_{ij})). \tag{56}$$

There are exactly $\binom{K}{2}$ distinct applications possible of the former identity in the first double sum of (54) and $\binom{K}{2}$ distinct applications of the latter identity in the second double sum of (54). After computing the difference and applying the identities to (54) we arrive at the required equality

$$\begin{aligned}\det(\varsigma^2\mathbf{I}) &= \sum_{i=1}^{K}\sum_{j=i+1}^{K}\sin^2(\Delta\theta_{ij}) \\ &= \frac{1}{2}\sum_{i=1}^{K}\sum_{j=i+1}^{K}(1 - \cos(2\Delta\theta_{ij})). \end{aligned} \tag{57}$$

Finally, substituting (57) into (51) yields (2).

REFERENCES

[1] R. D. Taranto, S. Muppirisetty, R. Raulefs, D. T. M. Slock, T. Svensson, and H. Wymeersch, "Location-aware communications for 5G networks," *IEEE Signal Process. Mag.*, vol. 31, pp. 102–112, Nov. 2014.

[2] A. Ghosh, A. Maeder, M. Baker, and D. Chandramouli, "5G evolution: A view on 5G cellular technology beyond 3GPP release 15," *IEEE Access*, vol. 7, pp. 127639–127651, Sep. 2019.

[3] M. Koivisto, A. Hakkarainen, M. Costa, P. Kela, K. Leppänen, and M. Valkama, "High-efficiency device positioning and location-aware communications in dense 5G networks," *IEEE Commun. Mag.*, vol. 55, no. 8, pp. 188–195, Aug. 2017.

[4] A. H. Sayed, A. Tarighat, and N. Khajehnouri, "Network-based wireless location: Challenges faced in developing techniques for accurate wireless location information," *IEEE Signal Process. Mag.*, vol. 22, no. 4, pp. 24–40, Jul. 2005.

[5] Y. Liu, X. Shi, S. He, and Z. Shi, "Prospective positioning architecture and technologies in 5G networks," *IEEE Netw.*, vol. 31, no. 6, pp. 115–121, Nov./Dec. 2017.

[6] N. Takbiri, A. Houmansadr, D. L. Goeckel, and H. Pishro-Nik, "Matching anonymized and obfuscated time series to Users' profiles," *IEEE Trans. Inf. Theory*, vol. 65, no. 2, pp. 724–741, Feb. 2019.

[7] S. Mazuelas, Y. Shen, and M. Win, "Spatiotemporal information coupling in network navigation," *IEEE Trans. Inf. Theory*, vol. 59, no. 2, pp. 940–949, Jul. 2010.

[8] K. Witrisal, P. Meissner, E. Leitinger, Y. Shen, C. Gustafson, F. Tufvesson, K. Haneda, D. Dardari, A. F. Molisch, A. Conti, and M. Z. Win, "High-accuracy localization for assisted living: 5G systems will turn multipath channels from foe to friend," *IEEE Signal Process. Mag.*, vol. 33, no. 2, pp. 59–70, Mar. 2016.

[9] A. Dammann, G. Agapiou, J. Bastos, L. Brunel, M. Garcia, J. Guillet, Y. Ma, J. Ma, J. Nielsen, L. Ping, R. Raulefs, J. Rodriguez, D. Slock, D. Yang, and N. Yi, "WHERE2 location aided communications," in *Proc. Eur. Wireless Conf.*, Apr. 2013, pp. 1–8.

[10] *Revision of the Commission's Rules to Ensure Compatibility With Enhanced 911 Emergency Calling Systems, Third Report and Order*, document 9 FCC RCD 17388, 1999.

[11] S. Sand, C. Mensing, Y. Ma, R. Tafazolli, X. Yin, J. Figueiras, J. Nielsen, and B. H. Fleury, "Hybrid data fusion and cooperative schemes for wireless positioning," in *Proc. IEEE 68th Veh. Technol. Conf.*, Sep. 2008, pp. 1–5.

[12] J. C. Aviles and A. Kouki, "Position-aided mm-wave beam training under NLOS conditions," *IEEE Access*, vol. 4, pp. 8703–8714, Nov. 2016.

[13] L. S. Muppirisetty, T. Svensson, and H. Wymeersch, "Spatial wireless channel prediction under location uncertainty," *IEEE Trans. Wireless Commun.*, vol. 15, no. 2, pp. 1031–1044, Feb. 2016.

[14] F. Cadger, K. Curran, J. Santos, and S. Moffett, "A survey of geographical routing in wireless ad-hoc networks," *IEEE Commun. Surveys Tuts.*, vol. 15, no. 2, pp. 621–653, Qua. 2013.

[15] *Stage 2 Functional Specification of User Equipment (UE) Positioning in NG-RAN*, document 3GPP TS 38.305, Release 15, v15.4.0, Jun. 2019.
[16] *5G System (5GS) Location Services (LCS); Stage 2*, document 3GPP TS 23.273, Release 16, v16.1.0, Sep. 2019.
[17] J. D. Roth, M. Tummala, and J. C. McEachen, "Efficient system geolocation architecture in next-generation cellular networks," *IEEE Syst. J.*, vol. 12, no. 4, pp. 3414–3425, Dec. 2018.
[18] *Feasibility Study on New Services and Markets Technology Enablers for Critical Communication; Stage 1*, document 3GPP TR 22.862, Release 14, v14.1.0, Sep. 2016.
[19] E. Baccelli, P. Jacquet, B. Mans, and G. Rodolakis, "Highway vehicular delay tolerant networks: Information propagation speed properties," *IEEE Trans. Inf. Theory*, vol. 58, no. 3, pp. 1743–1756, Mar. 2012.
[20] D. Tian, J. Zhou, and Z. Sheng, "An adaptive fusion strategy for distributed information estimation over cooperative multi-agent networks," *IEEE Trans. Inf. Theory*, vol. 63, no. 5, pp. 3076–3091, May 2017.
[21] H. ElSawy, E. Hossain, and M. Haenggi, "Stochastic geometry for modeling, analysis, and design of multi-tier and cognitive cellular wireless networks: A survey," *IEEE Commun. Surveys Tuts.*, vol. 15, no. 3, pp. 996–1019, 3rd Quart., 2013.
[22] J. G. Andrews, F. Baccelli, and R. K. Ganti, "A tractable approach to coverage and rate in cellular networks," *IEEE Trans. Commun.*, vol. 59, no. 11, pp. 3122–3134, Nov. 2011.
[23] *Physical Layer Aspects for Evolved Universal Terrestrial Radio Access (UTRA)*, document 3GPP TR 25.814, Release 7, v7.1.0, Sep. 2006.
[24] Z. Khalid and S. Durrani, "Distance distributions in regular polygons," *IEEE Trans. Veh. Technol.*, vol. 62, no. 5, pp. 2363–2368, Jun. 2013.
[25] M. Haenggi, "On distances in uniformly random networks," *IEEE Trans. Inf. Theory*, vol. 51, no. 10, pp. 3584–3586, Oct. 2005.
[26] S. Srinivasa and M. Haenggi, "Distance distributions in finite uniformly random networks: Theory and applications," *IEEE Trans. Veh. Technol.*, vol. 59, no. 2, pp. 940–949, Feb. 2010.
[27] F. Tong and J. Pan, "Random-to-Random nodal distance distributions in finite wireless networks," *IEEE Trans. Veh. Technol.*, vol. 66, no. 11, pp. 10070–10083, Nov. 2017.
[28] L. Miller, "Joint distributions of link distances," in *Proc. Conf. Inf. Sci. Syst.*, Mar. 2003, pp. 1–2.
[29] N. Levanon, "Lowest GDOP in 2-D scenarios," *IEE Proc.—Radar, Sonar, Navigat.*, vol. 147, no. 3, pp. 149–155, Jun. 2000.
[30] L. De Floriani, "A pyramidal data structure for triangle-based surface description," *IEEE Comput. Graph. Appl.*, vol. 9, no. 2, pp. 67–78, Mar. 1989.
[31] B. S. Baker, E. Grosse, and C. S. Rafferty, "Nonobtuse triangulation of polygons," *Discrete Comput. Geometry*, vol. 3, no. 2, pp. 147–168, Jun. 1988.
[32] H. Alikoski, "Über das sylvestersche vierpunktproblem," *Ann. Acad. Sci. Fenn.*, vol. 51, no. 7, pp. 1–10, 1939.
[33] H. Croft, K. Falconer, and R. Guy, *Unsolved Problems Geometry*. New York, NY, USA: Springer-Verlag, 1991.
[34] M. Pesavento, A. B. Gershman, and M. Haardt, "Unitary root-MUSIC with a real-valued eigendecomposition: A theoretical and experimental performance study," *IEEE Trans. Signal Process.*, vol. 48, no. 5, pp. 1306–1314, May 2000.
[35] S. Gong, H. Xiong, M. Peng, X. Ding, and H. Tang, "Joint DOD and DOA estimation for bistatic multiple-input multiple-output radar target discrimination based on improved unitary ESPRIT method," *IET Commun.*, vol. 12, no. 12, pp. 1397–1405, Jul. 2018.
[36] H. Jiang, J.-K. Zhang, and K. M. Wong, "Joint DOD and DOA estimation for bistatic MIMO radar in unknown correlated noise," *IEEE Trans. Veh. Technol.*, vol. 64, no. 11, pp. 5113–5125, Nov. 2015.
[37] I. Güvenç and C.-C. Chong, "A survey on TOA based wireless localization and NLOS mitigation techniques," *IEEE Commun. Surveys Tuts.*, vol. 11, no. 3, pp. 107–124, 3rd Quart., 2009.
[38] M. DeGroot and M. Schervish, *Probability and Statistics*, 4th ed. London, U.K.: Pearson, 2012.
[39] *Further Advancements for E-UTRA Physical Layer Aspects*, document 3GPP TR 36.814, Release 9, v9.2.0, Mar. 2017.
[40] J. G. Andrews, "Seven ways that HetNets are a cellular paradigm shift," *IEEE Commun. Mag.*, vol. 51, no. 3, pp. 136–144, Mar. 2013.

JOHN D. ROTH (Senior Member, IEEE) received the B.S. degree in electrical engineering from the U.S. Naval Academy, Annapolis, MD, USA, in 2004, and the M.S. and Ph.D. degrees in electrical engineering from the Naval Postgraduate School, Monterey, CA, USA, in 2012 and 2016, respectively.

He is currently an Assistant Professor of electrical and computer engineering with the Naval Postgraduate School. His research interests include communications, signal processing, and stochastic geometry.

MURALI TUMMALA (Senior Member, IEEE) received the M.S. and Ph.D. degrees in electrical engineering from the IIT Bombay, India.

He is currently a Professor of electrical and computer engineering with the Naval Postgraduate School, Monterey, CA, USA. His teaching and research interests include wireless networking, communications, and signal processing.

JOHN C. MCEACHEN (Member, IEEE) received the B.S.E.E. degree from the University of Notre Dame, the M.S.E.E. degree from the University of Virginia, and the M.Phil. and Ph.D. degrees in electrical engineering from Yale University.

He is currently a Distinguished Professor of electrical and computer engineering with the Naval Postgraduate School, Monterey, CA, USA. His teaching interests include computer networks, communications systems, and cyber operations. His research interests include managing routing in computer networks, wireless networking protocols, patternless intrusion detection, and steganographic communications. He is a retired Commander of the U.S. Naval Reserves and is a member of the Tau Beta Pi and Eta Kappa Nu. He is the former Director of the Naval Postgraduate School Center for Cyber Warfare. He was the Founding Editor-in-Chief of *Military Cyber Affairs* and the *Journal of the Military Cyber Professionals Association*. He was a member of the Editorial Board of the *International Journal of Electronic Security and Digital Forensics* (Inderscience).